RELIABILITY ANALYSIS OF A POWER ELECTRONIC INTEGRATED GENERATOR FOR WIND ENERGY CONVERSION SYSTEMS

BY

ISAAC LAWANSON

THESIS

Submitted in partial fulfillment of the requirements
for the degree of Master of Science in Electrical and Computer Engineering
in the Graduate College of the
University of Illinois Urbana-Champaign, 2022

Urbana, Illinois

Adviser:

Professor Alejandro Domínguez-García

ABSTRACT

This thesis presents a novel design for off-shore wind turbines. Reliability analysis of AC to DC power converter architectures that are utilized in this wind energy conversion system is performed with Markov reliability and availability modeling. The three architectures under investigation are: the baseline, based on a sole active rectifier; the proposed, comprising an active rectifier and three passive rectifiers; and the proposed outfitted with electromechanical bypass relay switches. The models are used to determine reliability, system failure rate, and availability of all three architectures. Sensitivity analysis of various component failure and repair rates on the reliability metrics just mentioned is also performed. An averaged high-order model of the wind-turbine is presented and reduced using singular perturbation analysis. The reduced-order model is used to calculate the expected power output of the off-shore wind turbine.

To my parents and sister, for their love and support.

ACKNOWLEDGMENTS

I would like to thank my adviser, Prof. Alejandro Domínguez-García, for the support he provided, and the knowledge he imparted to me over the last two years. I am grateful for his approach to research problems, ensuring that I understand what I am working on and why it is important. I am also thankful to all the ECE Illinois professors and staff in the Power and Energy Systems group for providing the resources I needed to achieve success.

I would like to thank Macks, Sidd, T.G., Tope, Olaolu, Daniel, Talal and all the other students in the Power and Energy Systems group for making this journey to obtain a master's degree not only fun and entertaining, but also welcoming and safe, especially during a global pandemic.

Finally, I would like to thank Rachel for being my rock over the past few years, and my family for encouraging me to reach for my goals regardless of the circumstance. I love you all.

TABLE OF CONTENTS

CHAPTER 1

INTRODUCTION

Sustainable Development Goal 7, from the United Nations Department of Economic and Social Affairs, is to ensure access to affordable, reliable, sustainable and modern energy for all by 2030 [1]. Fossil fuels, the main source of energy production for the worldwide economy, are a major cause of environmental problems, namely, global warming, because of the increasing CO_2 emissions. While the world pushes for more energy production to raise the economic standard of living for those in developing countries, these environmental problems persist. Hence, there has been a push to search for alternative energy suppliers for power generation, and renewable energy production has been on an increasing trend on the global scale over the last few decades [2]. Renewable energy sources like wind and solar generate minimal global warming emissions, addressing these concerns. In addition, they could also provide economic benefit as the cost of this energy is free and the majority of investment into these technologies is in the development, installation and maintenance phases.

Wind energy has become one of the fastest growing sources of renewable energy used for electrical power generation around the world [2,3]. This trend is not slowing down as the US Department of Energy targets 20% wind energy based production by 2030 [4]. The majority of the wind energy produced in the world is from on-shore wind farms where there is limited potential for growth [5]. On the other hand, there is high off-shore wind energy potential globally because of the higher and more consistent wind speed regimes that exist at lower altitudes compared to regimes over land. This also results in steadier rate of power generation compared to onshore wind farms [6]. Offshore wind turbines with power ratings in the range of 10-14 MW like GE Haliade X, Gamesa 10X, and Vestas V164 have been designed [7–9]; these ratings are much higher than those of on-shore alternatives..

The direct-drive permanent magnet synchronous generator (PMSG) with

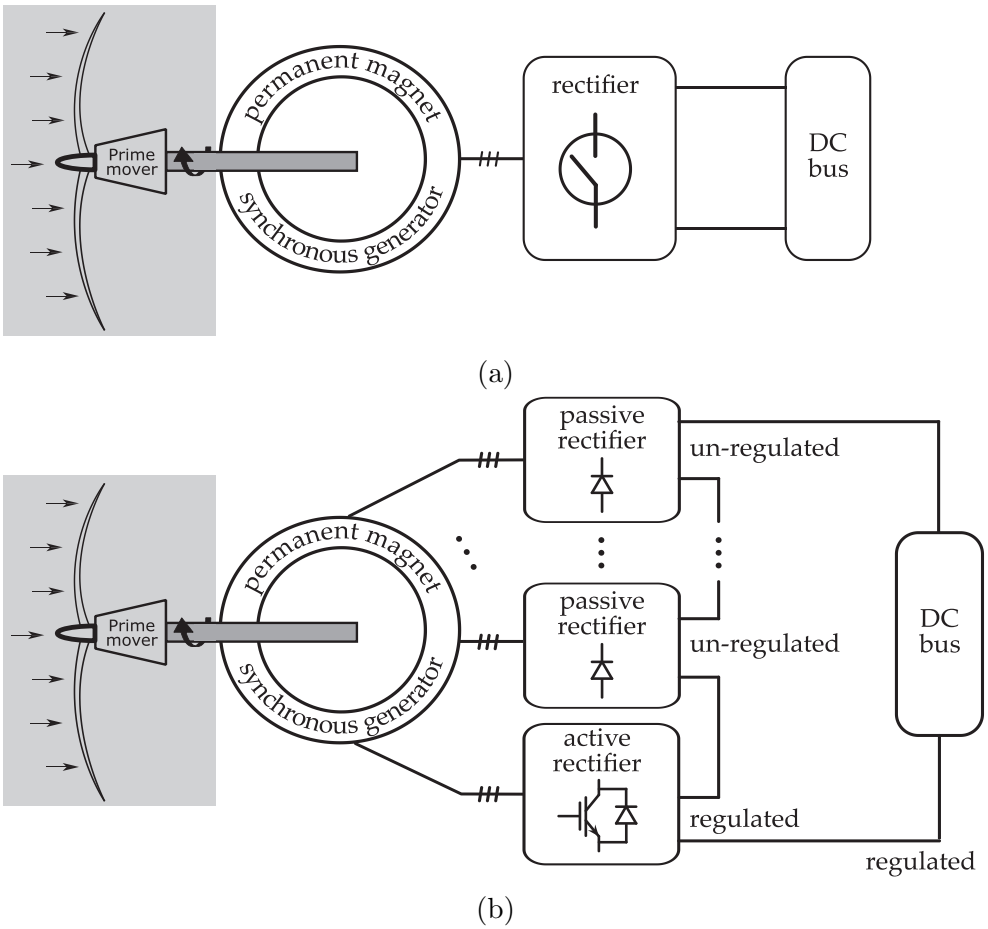

Figure 1.1: Power-electronic-integrated generators for wind energy conversion systems.

full power converters, like the structure seen in Fig. 1.1(a), is the standard design for wind turbines in off-shore environments [10–15]. Figure 1.1(b), on the other hand, shows a novel design with an integrated generator-rectifier system that reduces the power rating requirements of the active rectifier with the addition of passive rectifiers [16, 17]. This novel design and its characteristics will be the focus of this thesis.

The mechanical power on the turbine shaft is converted to AC electrical power by a multiport PMSG. Each port is connected to either a passive or an active rectifier for AC–DC conversion. The DC outputs of the rectifiers are connected serially to form a high-voltage DC bus. Each rectifier supports only a fraction of the total DC bus voltage, reducing the voltage across the active rectifier. As a result, 60% of the total power is processed on passive rectifiers. There is a 47% reduction in conversion loss and a 32% switch

VA-rating at the rated operating conditions. This results in improvement of power density and efficiency in the system [18]. Power-flow control is achieved with the active rectifier which also allows for maximum power point tracking (MPPT). The DC bus voltage ripple is reduced by shifting the phases of different ac ports that are feeding the passive rectifiers.

While the advantages of this technology seem clear, there is a need to assess its reliability as the next major cost for operating an off-shore wind farm with this wind energy conversion system, after development and installation, will be operation and maintenance costs [19]. Using reliability metrics, its energy output can be anticipated to ensure proper location of the wind turbines and power allocation planning. The key contribution of this thesis is to analyze the reliability and availability of this novel approach to power-electronic-integrated generators for wind energy conversion systems and to explore new techniques for power output analysis of off-shore wind turbines.

1.1 Converter Architecture Description

AC-to-DC power converter architectures for wind energy conversion systems are investigated in this thesis. A baseline architecture is introduced in this section, as well as two proposed architectures, both of which contain passive rectifiers, and one of which contains an additional bypass mechanism to isolate failed passive rectifiers. These differences in architecture will be explored in further chapters as they impact the system's reliability, availability, failure rate and power output.

1.1.1 Baseline Architecture

This power converter architecture will be referred to as Architecture 1 in this thesis. It is based on the fully-rated power converter that is presented in [20]. It comprises an active rectifier and other auxiliary systems, such as cooling systems, lubrication systems, and rectifier control modules. The active rectifier differs from the other architectures; therefore, it will be the focus of the analysis. The active rectifier is composed of six active switches and a film capacitor as seen in Fig. 1.2(a). This architecture is not *fault tolerant,* i.e., it cannot withstand any single component failure. When an

active switch or the capacitor fails, the converter system is in a failed state.

1.1.2 Integrated Passive Rectifier Architecture

This power converter architecture will be referred to as Architecture 2 in this thesis. It is based on the megawatt-scale power converter that is presented in [21]. It comprises an active rectifier, three passive rectifiers and the other auxiliary systems. The active rectifier is composed of six diodes, twelve active switches, and two film capacitors, while the passive rectifier is composed of six diodes as seen in Fig. 1.2(b). This active rectifier is adjusted with a neutral-point-clamped (NPC) topology [22] that reduces the voltage across the diodes, switches and capacitors by half [21]. This architecture, like Architecture 1, is *not fault tolerant*. When an active switch, diode or capacitor fails, the converter system is in a failed state.

1.1.3 Integrated Passive Rectifier Architecture with Bypass Mechanism

This power converter architecture will be referred to as Architecture 3 in this thesis. It is similar to Architecture 2 with the addition of electromechanical bypass relay switches. It comprises an active rectifier, three passive rectifiers, nine bypass relay switches and the other auxiliary systems as seen in Fig. 1.2(c). The bypass mechanism isolates failed passive rectifiers from the converter architecture, allowing the system to continue operating. This architecture is fault tolerant against failures in its passive rectifiers but it is not fault tolerant against failures in the active rectifier.

Figure 1.2(c) shows the passive rectifier with bypass mechanism. When a diode in a passive rectifier fails, the relay switches change states; i.e., the open switch (B) closes and the closed switches (A1 and A2) open to isolate the passive rectifier associated with the failed diode. The actions of the relay switches cause the system to remain operational when one passive rectifier fails but it can only produce a maximum of three-quarters of the rated power output. When two passive rectifiers fail, the system's rated power output is halved. When three fail, only a quarter of the rated power output can be produced.

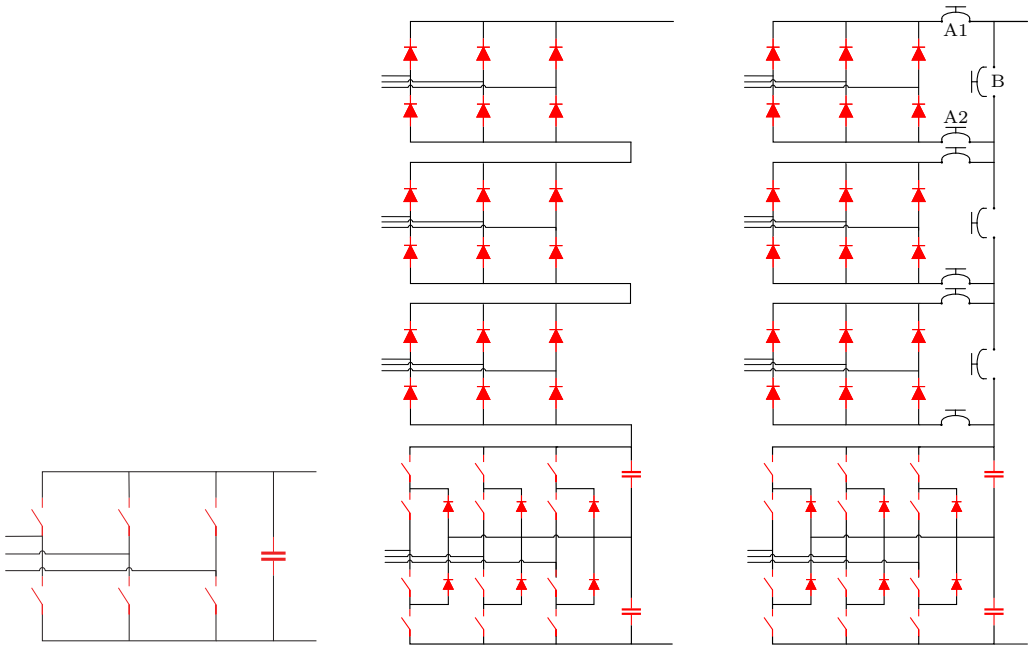

Figure 1.2: Schematic diagram of the (a) baseline, (b) integrated passive rectifier, and (c) integrated passive rectifier architecture w/ bypass mechanism.

1.2 Summary

This thesis contains four additional chapters. In chapter 2, a primer on Markov reliability modeling is presented, introducing reliability and system failure rate as metrics to measure performance of the integrated generator-rectifier system. Markov reliability models are created for each converter architecture and numerically analyzed to quantify their performance. Additionally, analysis is performed to determine the effect of each component within the architectures on the reliability and failure rate. In chapter 3, Markov availability models with varying repair strategies are created for each converter architecture. Availability, and sensitivity of the availability relative to each component failure and repair rate, is then calculated. In chapter 4, an averaged high-order model of the integrated generator-rectifier is described. A technique for model-order reduction, singular perturbation analysis, is introduced and used to develop a reduced-order model of the integrated generator-rectifier system. This new model is numerically compared to the averaged high-order model from which it was obtained.. In

chapter 5, an approximation of the wind profile, the Weibull distribution, is presented and used to determine the expected power output of the off-shore wind turbine over a 30 year period. In chapter 6, the thesis is summarized and concluded.

CHAPTER 2

MARKOV RELIABILITY MODELS

2.1 Primer

Let $Q = \{Q(t), t \geq 0\}$ denote a Markov chain describing the stochastic behavior of a system subject to component failures and repairs. Assume that $Q(t)$ takes values in a finite set $\mathcal{Q} = \{1, 2, ..., n\}$, where 1 indexes the nominal, non-faulty system configuration, and $2, ..., n$, index system configurations as determined by the components that are operating in their nominal mode, and the components that have transitioned from operating in their nominal to their failed mode, and the chronological order in which these transitions occurred. Thus, transitions among the elements of $\mathcal{Q}$ are associated with the failure of one or more components or repair actions triggered to correct such failures.

Let $\pi_i(t)$, $t \geq 0$, denote the probability that the system is in configuration i at time t, and define the corresponding probability vector as $\pi(t) = \left[\pi_1(t), \pi_2(t), ..., \pi_n(t)\right]^\top$. The evolution of $\pi(t)$ is governed by the Chapman-Kolmogorov equation

$$\dot{\pi}(t) = G\pi(t), \tag{2.1}$$

where G denotes the generator of Q (see, e.g., [23], [24]), $\pi_1(0) = 1$, and $\pi_j(0) = 0$, $j = 2, ..., n$. The entries of G are as follows:

- $G_{i,j}$, $i \neq j$, which we denote by $g_{i,j}$, is determined by the failure rates or repair rates associated with the components involved in the transition from configuration j to configuration i.
- $G_{j,j} = -\sum_{i \neq j}^{n} g_{i,j}$.

The reader is referred to [25] for a detailed discussion on how to construct $\mathcal{Q}$ and G.

In a Markov reliability model, there are some absorbing states, i.e., states with no transition out. These states correspond to configurations in which the system is nonoperational. The reliability of a system at time t, $R(t)$, can be defined as the probability that the non-repairable system is operating at time t, i.e., the sum of the probabilities of configurations i, where the non-repairable system is operational. A Markov reliability model describes the stochastic behavior of a system before its first failure.

Let T denote a continuous random variable describing the time to failure of a system, with continuously differentiable cumulative density function, $F_T(t)$, and probability density function, $f_T(t)$. Then, since $R(t) = \Pr(T \geq t)$, it follows that

$$F_T(t) = 1 - R(t), \tag{2.2}$$

$$\begin{aligned} f_T(t) &= \frac{dF_T(t)}{dt}, \\ &= -\dot{R}(t). \end{aligned} \tag{2.3}$$

Let λ_{sys} denote the failure rate of the system; then, it follows that

$$\begin{aligned} \lambda_{sys}(t) &= \frac{f_T(t)}{1 - F_T(t)}, \\ &= \frac{-\dot{R}(t)}{R(t)}. \end{aligned} \tag{2.4}$$

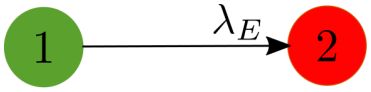

Figure 2.1: Single-component Markov reliability model. The green state indicates the system is operational. The red state indicates the system is not operational.

Example: Consider a system comprising a single component and denote by E an event that causes it to fail. This system can only adopt two possible configurations: one in which the component is operating and one in which the component has failed; thus $Q = \{1, 2\}$. Figure 2.1 shows the state-transition diagram of the Markov reliability model associated with this system. From

Fig. 2.1, the generator for this Markov reliability model is given by

$$G = \begin{bmatrix} -\lambda_E & 0 \\ \lambda_E & 0 \end{bmatrix}, \tag{2.5}$$

where λ_E is the component failure rate. By solving (2.1) for $\pi_1(0) = 1$, and $\pi_2(0) = 0$, we obtain

$$\pi_1(t) = e^{-\lambda_E t}, \tag{2.6}$$

$$\pi_2(t) = 1 - e^{-\lambda_E t}, \tag{2.7}$$

and, for any mission time t_m, the reliability of the system, $R(t_m)$, can be computed as

$$\begin{aligned} R(t_m) &= \pi_1(t_m), \\ &= e^{-\lambda_E t_m}. \end{aligned} \tag{2.8}$$

The failure rate of the system, λ_{sys}, can be computed as

$$\begin{aligned} \lambda_{sys}(t_m) &= -\frac{dR(t_m)/dt}{R_T(t_m)}, \\ &= \lambda_E. \end{aligned} \tag{2.9}$$

2.2 Component Failure Rates

As described in Chapter 1, each power converter architecture has capacitors, passive and/or active switches and film capacitors. Architecture 3 has bypass relay switches.[1]

2.2.1 Film Capacitors

The equation for the capacitance degradation curve of a film capacitor that is used in this work is

[1] In this thesis, the failure rate of the bypass relay mechanism is neglected as it is less frequently active than other electronic components.

$$C = 1.00301 - 0.00039 * \exp\left(\frac{0.00166}{30}t\right), \tag{2.10}$$

where C denotes the normalized capacitance, and t denotes time in hours. It was derived by adopting and modifying the result presented in [26]. The life expectancy of film capacitors, as reported in electronic component datasheets [27], is typically greater than 100,000 hours, but the result presented in [26] infers that the life expectancy of the film capacitor is less than 2,000 hours. This discrepancy is due to accelerated degradation testing of film capacitors in [26]. In order to match the film capacitor life expectancy values reported in component datasheets, the result's rate of decay in [26] was reduced by a factor of 30, and (2.10) is the resulting expression.

The capacitance degradation is plotted in Fig. 2.2 along with a quantized version obtained by setting the maximum difference between the actual value of C and the quantized value to be 0.02 per unit. Then, we assume that the time it takes to transition from a quantization level to the next is random and can be characterized by some transition rate.

Let $\lambda_c^{(i)}$ be the failure rate associated with each stage of the capacitor degradation model, where

- $\lambda_c^{(1)}$: The failure rate that determines the transition between nominal capacitance and 0.97 of its value.
- $\lambda_c^{(2)}$: The failure rate that determines the transition between 0.97 of the nominal capacitance and 0.935 of the same value.
- $\lambda_c^{(3)}$: The failure rate that determines the transition between 0.935 of the nominal capacitance and 0.895 of the same value.

The operating voltage of the active rectifier in Architecture 1 is larger than that of the active rectifier in Architectures 2 and 3, with ratio, r. Hence, the capacitance failure rates are affected as follows [28], [29]:

$$\frac{\lambda_c^{(1)}}{\widehat{\lambda}_c^{(1)}} = r^{\alpha}, \quad \frac{\lambda_c^{(2)}}{\widehat{\lambda}_c^{(2)}} = r^{\alpha}, \quad \frac{\lambda_c^{(3)}}{\widehat{\lambda}_c^{(3)}} = r^{\alpha}, \tag{2.11}$$

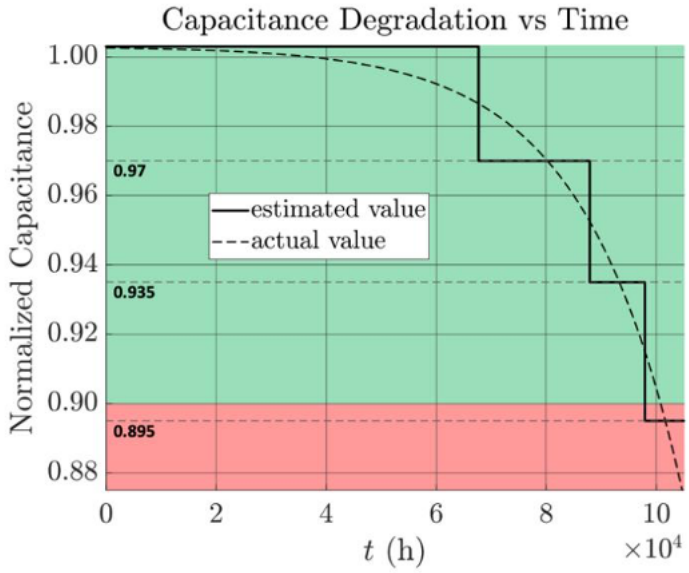

Figure 2.2: Capacitance degradation curve. The green area shows when the capacitor is considered operational. The red area shows when the capacitor is considered not operational.

where $\alpha \in [3, 5]$ and $\widehat{\lambda}_c^{(i)}$ is the failure rate associated with each stage of the capacitor degradation model in Architectures 2 and 3.

2.2.2 Active Switches

Let λ_{as} be the active switch failure rate. The voltage ratio, r, also affects the active switch failure rate as follows:

$$\frac{\lambda_{as}}{\widehat{\lambda}_{as}} = r^{\alpha}, \tag{2.12}$$

where $\alpha \in [3, 5]$ and $\widehat{\lambda}_{as}$ is the failure rate of the active switch in Architectures 2 and 3.

2.2.3 Passive Switches

Passive switches are components in the active and passive rectifiers of Architectures 2 and 3. Let λ_d be the passive switch failure rate. The voltages experienced by the passive switches in the passive rectifiers is higher than

that of the passive switches in the active rectifier, with ratio r_{ps}. This also affects the passive switch failure rate as follows:

$$\frac{\lambda_d}{\widehat{\lambda}_d} = r_{ps}^{\alpha}, \tag{2.13}$$

where $\alpha \in [3, 5]$ and $\widehat{\lambda}_d$ is the failure rate of the passive switch in the active rectifiers of Architectures 2 and 3.

2.2.4 Auxiliary Systems

Let λ_{cs2} denote the failure rate of the cooling system, λ_{cm}, the control modules, λ_{ps}, the protection system, and λ_{os}, the other sub-assemblies. We assume that, for Architectures 2 and 3, the failure rates of the cooling system and the control modules are denoted by $\widehat{\lambda}_{cs2}$ and $\widehat{\lambda}_{cm}$, respectively, where

$$\frac{\lambda_{cs2}}{\widehat{\lambda}_{cs2}} = r^{\alpha}, \quad \frac{\lambda_{cm}}{\widehat{\lambda}_{cm}} = r^{\alpha}. \tag{2.14}$$

2.3 Description

Failure rates of the different components will be used to populate the Chapman-Kolmogorov equation in order to build the reliability models of the different architectures. Their solution will give the system's reliability and failure rate.

2.3.1 Architecture 1

The active rectifier is in a failed state when one or more of the active switches has failed or if the film capacitor has degraded by 10 percent or more. For this architecture, there are four failure events as described in Table 2.1; these are labeled as AR_1, $C1$, $C2$ and $C3$. Let λ_{ar} denote the failure rate of the active rectifier without the failure rate of the capacitor, i.e.

$$\lambda_{ar} = 6\lambda_{as} + \lambda_{cs2} + \lambda_{cm} + \lambda_{ps} + \lambda_{os}. \tag{2.15}$$

Accordingly, the Markov reliability model state-transition diagram for Architecture 1 is depicted in Fig. 2.3. Let $\pi_i(t)$ denote the probability that Architecture 1 is in configuration i. The evolution of $\pi_i(t)$ for $i = 1, 2, ..., 7$, is described by the Chapman-Kolmogorov equation from Section 2.1. The system-level failure rate of the active rectifier and the converter failure rate, i.e. the system-level failure rate without the auxiliary systems, are then calculated.

2.3.2 Architecture 2

The active rectifier is in a failed state when one or more of the active switches or diodes has failed, or if any of the two film capacitors has degraded by 10 percent or more. A passive rectifier is in a failed state when one or more diodes has failed. The converter system is in a failed state when an active rectifier or one or more of the passive rectifiers has failed. Architecture 1 and 2 both utilize active rectifiers. For this architecture, there are four failure events as seen in Table 2.1, E, $C1$, $C2$ and $C3$. Let $\widehat{\lambda}_{ar}$ denote the failure rate of the active rectifier without the failure rate of the capacitors, i.e.

$$\widehat{\lambda}_{ar} = 12\widehat{\lambda}_{as} + 6\widehat{\lambda}_{d} + \widehat{\lambda}_{cs2} + \widehat{\lambda}_{cm} + \lambda_{ps} + \lambda_{os}, \tag{2.16}$$

and let λ_e denote the failure rate of the active rectifier without the failure rate of the capacitors and the failure rates of the passive rectifiers, i.e.

$$\lambda_e = \widehat{\lambda}_{ar} + 18\lambda_d. \tag{2.17}$$

Accordingly, the Markov reliability model state-transition diagram for Architecture 2 is depicted in Fig. 2.3. The evolution of $\pi_i(t)$ for $i = 1, 2, ..., 7$, is described by the Chapman-Kolmogorov equation from Section 2.1. The system-level failure rate of the active rectifier and the converter failure rate are then calculated.

2.3.3 Architecture 3

The active and passive rectifiers still fail in the same ways as Architecture 2, but with the ability to isolate failed passive rectifiers. A failure in a passive rectifier does not mean converter system failure. Note again that if the active rectifier fails at any point, the converter system fails, regardless of the failure states of the passive rectifiers. For this architecture, there are four failure events, labeled as AR_2, $C1$, $C2$, and $C3$, which are described in Table 2.1. $\widehat{\lambda}_{ar}$ denotes the denote the failure rate of the active rectifier without the failure rate of the capacitor. Accordingly, the Markov reliability model state-transition diagram for Architecture 3 is depicted in Fig. 2.4. The evolution of $\pi_i(t)$ for $i = 1, 2, ..., 28$, is described by the Chapman-Kolmogorov equation from Section 2.1. The system-level failure rate of the active rectifier and the converter failure rate are then calculated.

Table 2.1: Failure Event Description

Event	Description	Failure Rate
AR_1	At least 1 of 6 active switches fails or one of the auxiliary systems fails	λ_{ar}
E	At least 1 of 12 active switches fails, 1 of 24 diodes fails, or one of the auxiliary systems fails	λ_e
AR_2	At least 1 of 12 active switches fails, 1 of 6 diodes fails in the active rectifier, or one of the auxiliary systems fails	$\widehat{\lambda}_{ar}$
$C1$	The capacitor degrades to 0.97 of its nominal value	$\lambda_c^{(1)}$
$C2$	The capacitor degrades to 0.935 of its nominal value	$\lambda_c^{(2)}$
$C3$	The capacitor degrades to 0.895 of its nominal value	$\lambda_c^{(3)}$

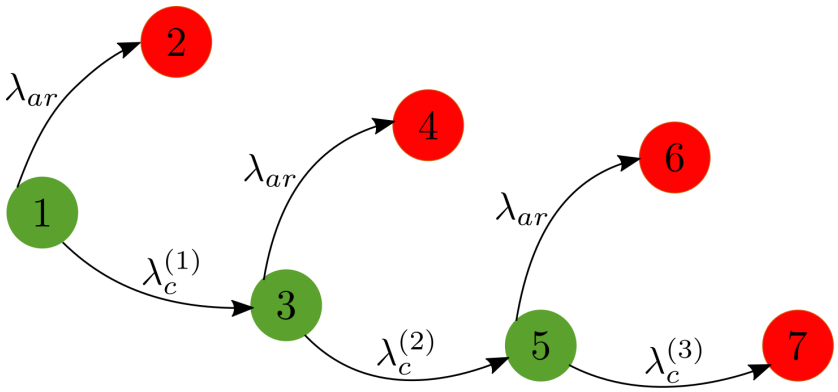

Figure 2.3: Markov reliability model state-transition diagram for Architecture 1 and 2 is of this form. Green states indicate sequences of failures in which the active rectifier is operational. Red states indicate sequences of failures in which the active rectifier is not operational.

2.4 Numerical Results

The values in Table 2.2 are all obtained from [20], [30] and from Fig. 2.2 and are all in units of failures/year. Employing the conservative assumptions that $r = 3.33$ and $\alpha = 3$ for all the components in the auxiliary systems, $r = 6.66$ and $\alpha = 3$ for active switches and capacitors, and $r_{ps} = 2$ and $\alpha = 3$ for the passive switches in the active rectifier, we can calculate the new failure rates for Architectures 2 and 3. All the calculations in this subsection are done for $t = 30$ years.

Table 2.2: Failure Rates

Failure Rates	Architecture 1	Architecture 2
λ_{as}	0.0215	7.28e-5
λ_d in AR	n/a	0.0002
λ_d	n/a	0.0016
$\lambda_c^{(1)}$	0.1294	0.00044
$\lambda_c^{(2)}$	0.4334	0.0015
$\lambda_c^{(3)}$	0.8725	0.0030
λ_{cs2}	0.2620	0.0071
λ_{cm}	0.1610	0.0044
λ_{ps}	0.0300	0.0300
λ_{os}	0.0120	0.0120

As seen in Table 2.3, the failure rate of the converter architecture with

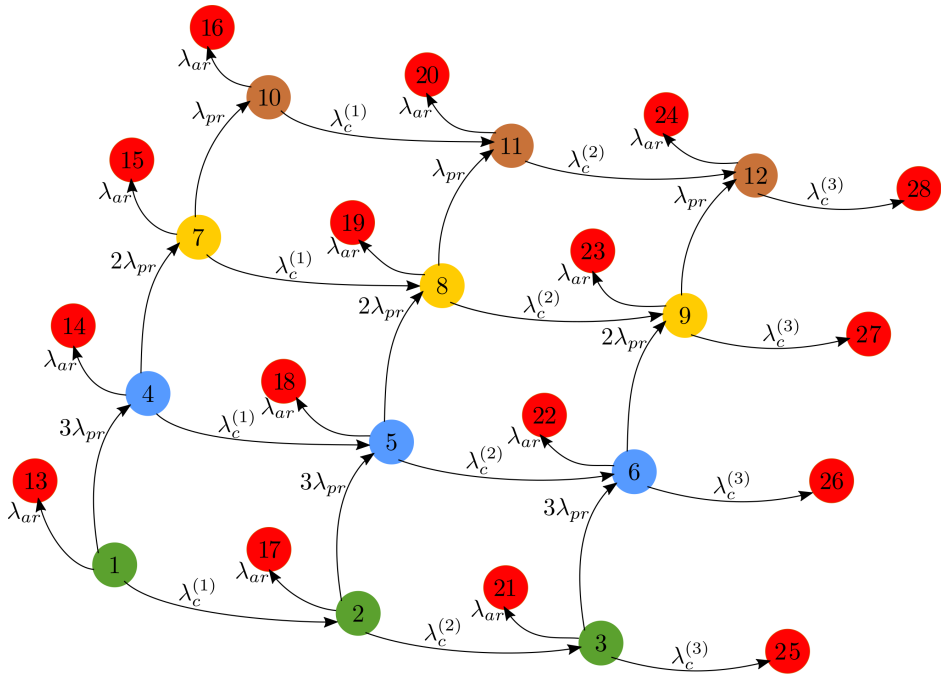

Figure 2.4: Markov reliability model state-transition diagram for Architecture 3. Green states (Configurations 1, 2 and 3) indicate sequences of failures in which the system is operational, and all the power is delivered. Blue states (Configurations 4, 5 and 6) indicate sequence of failures in which the system is operational, and three quarters of the power is delivered. Yellow states (Configurations 7, 8 and 9) indicate sequence of failures in which the system is operational, and half of the power is delivered. Orange states (Configurations 10, 11 and 12) indicate sequence of failures in which the system is operational, and just one quarter of the power is delivered. Red states (Configurations 13 to 28) indicate sequences of failures in which the active rectifier is not operational, so no power is delivered. By solving the Markov reliability model, the probability of occurrence of every sequence of failures at any given instant can be computed.

or without the additional sub-assemblies, like cooling systems and control modules, is significantly improved when comparing Architecture 1 with 2, because the addition of passive rectifiers reduces the input voltage on the active rectifier and the additional sub-assemblies in the converters. The failure rate of Architecture 3 is even lower than Architecture 2 because a failure in the passive rectifiers does not result in failure of the whole system. This was discussed in more detail in Section 2.3.3. Figure 2.5 shows the evolution of the system-level failure rate of all the different converter architectures studied in this thesis. It is observed that Architectures 2 and 3 present an

order of magnitude reduction in failure rates when they are compared with Architecture 1.

Table 2.3: Converter Failure Rates

Failure Rates	Architecture 1	Architecture 2	Architecture 3
Converter	0.2584	0.0309	0.0021
System-level	0.7234	0.0844	0.0556

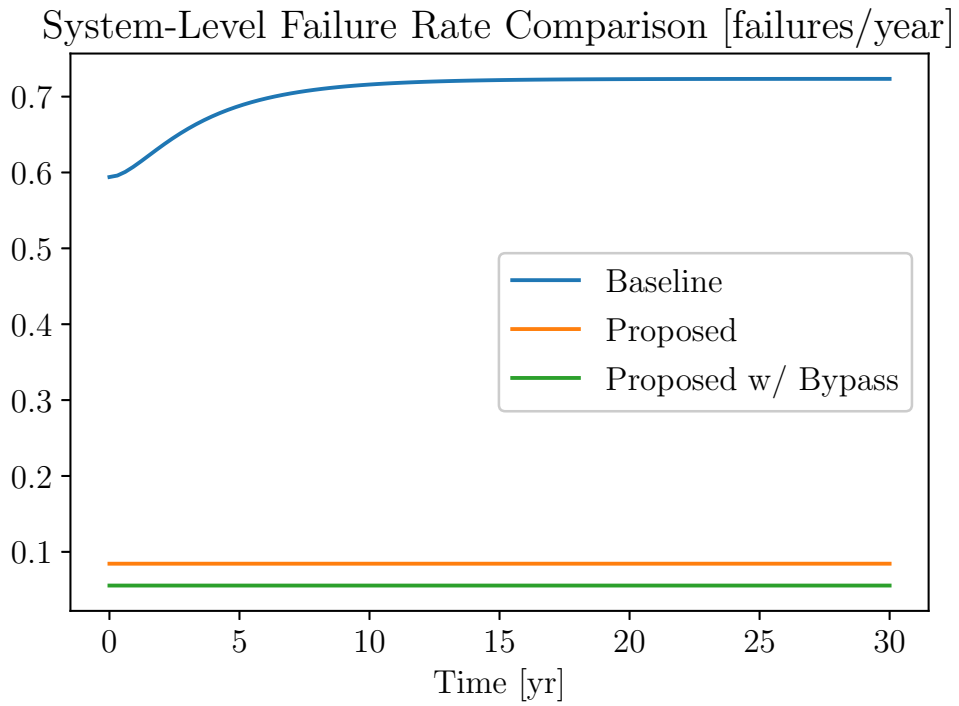

Figure 2.5: A comparison of the system-level failure rates for all the converter architectures.

2.5 Sensitivity Analysis

For the Markov reliability model, sensitivity analysis is done on the system-level failure rate of each converter architecture by first scaling the failure rate under consideration by κ, the failure rate multiplier, while holding all other failure rates constant, κ ranging from 1 to 10. Then, the same Chapman-

Kolmogorov equation discussed in Section 2.1 is used to calculate the system-level failure rate. This process is done for the failure rates λ_{as}, $\lambda_c^{(1)}$, $\lambda_c^{(2)}$, $\lambda_c^{(3)}$, and λ_d, as these failure rates are primarily altered due to the different designs for every converter architecture. We can then compare the impact of the scaled failure rates on the system-level failure rate.

In Fig. 2.6, it is clear that the failure rate with the biggest effect on the system-level failure rate is λ_{as}, the failure rate of each active switch, causing an increase of 160%. The effect of $\lambda_c^{(1)}$ approaches an asymptote, causing an increase of 42% while the effects of $\lambda_c^{(2)}$ and $\lambda_c^{(3)}$ are negligible when increased by a magnitude of 10.

There is significant reduction in the magnitude of the failure rate of the system compared to Fig. 2.6, as shown in Fig. 2.7, because of the changes to the converter architecture. With the abundance of diodes in this new architecture, the effect of λ_d is much more significant (a failure rate increase of 320%) than the failure rates of the capacitor and active switches, although λ_{as} clearly has more effect than $\lambda_c^{(1)}$, $\lambda_c^{(2)}$ and $\lambda_c^{(3)}$.

With the system failure rate further reduced by including a bypass mechanism, λ_d and λ_{as} have the strongest effect, with diodes having a slightly higher influence because of the magnitude of λ_d compared to λ_{as}, as shown in Fig. 2.8. The scaling up of λ_d by 10 results in the failure rate increase of 19%. The capacitor values behave as discussed in earlier sections.

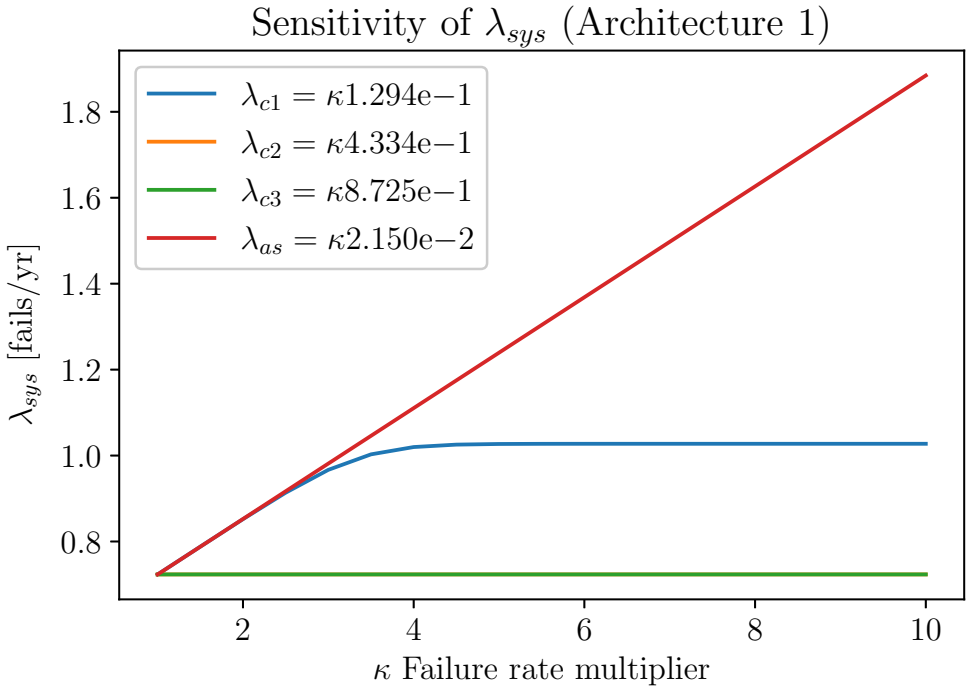

Figure 2.6: Sensitivity of the system-level failure rate for Architecture 1 with respect to varying failure rates at $t = 30$ years.

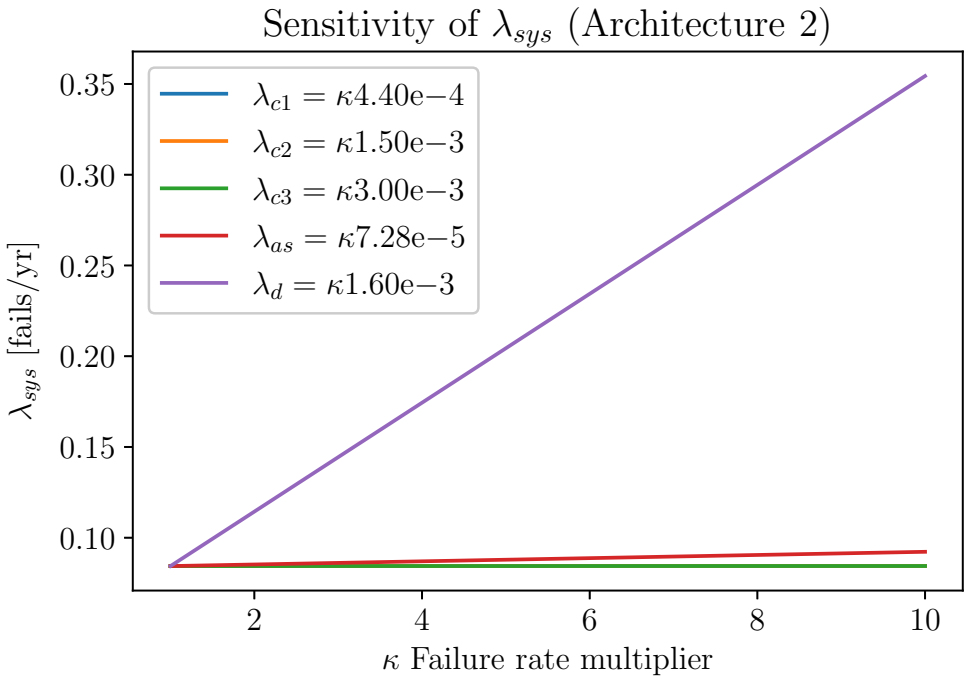

Figure 2.7: Sensitivity of the system-level failure rate for Architecture 2 with respect to varying failure rates at $t = 30$ years.

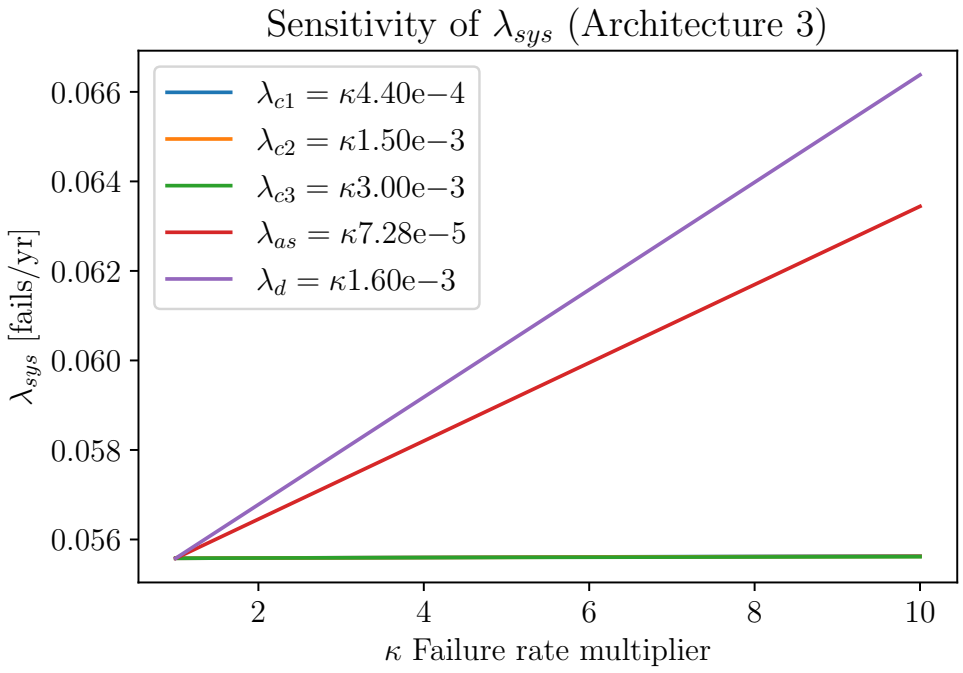

Figure 2.8: Sensitivity of the system-level failure rate for Architecture 3 respect to varying failure rates at $t = 30$ years.

CHAPTER 3

MARKOV AVAILABILITY MODEL

3.1 Primer

As stated in chapter 2, in a Markov reliability model, there are some absorbing states, i.e., states with no transition out. In a Markov availability model, however, there are no absorbing configurations. Nonoperational states of the system still exist but every configuration can be transitioned out of via failures and/or repairs. The availability of a system at time t, $A(t)$, can be defined as the sum of the probabilities of configurations i, where the repairable system is operational. The Chapman-Kolmogorov equation (2.1) is used to calculate availability with the addition of repair rates to the generator matrix, G.

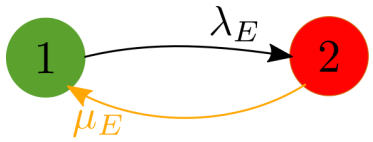

Figure 3.1: Single-component Markov availability model. The green state indicates the system is operational. The red state indicates the system is not operational.

Example: Consider a system comprising a single component and denote by E an event that causes it to fail. This system can only adopt two possible configurations, one in which the component is operating, and one in which the component has failed; thus $Q = \{1, 2\}$. Figure 3.1 shows the state state-transition diagram of the Markov reliability model associated with this system. From Fig. 3.1, the generator for this Markov reliability model is given by

$$G = \begin{bmatrix} -\lambda_E & \mu_E \\ \lambda_E & -\mu_E \end{bmatrix}, \tag{3.1}$$

where μ_E is the component repair rate. The availability of the system, $A(t_m)$, for any mission time t_m, can be computed as

$$\begin{aligned} A(t_m) &= \sum_{i \in \mathcal{Q}_o} \pi_i(t_m), \\ &= \pi_1(t_m), \\ &= \frac{\mu_E + \lambda_E e^{-\lambda_E t_m - \mu_E t_m}}{\mu_E + \lambda_E}. \end{aligned} \tag{3.2}$$

3.2 Description

Failure and repair rates of the different components will be used to populate the Chapman-Kolmogorov equation in order to build the reliability models of the different architectures. Their solution will give the system's availability.

3.2.1 Architecture 1

The characteristic that all of the repair strategies have in common is that there is a repair from states where the failure occurred because of the switches or the auxiliary components, to the prior state where the system was, i.e., a transition from state 2 to 1, 4 to 3 and 6 to 5 at a rate of μ_{ar} repairs/year as seen in Fig. 3.2. For the capacitor, these are the repair strategies considered:

1. Repairing the system just when the capacitor is down, i.e., repairing the capacitor just when it reaches state 7, at a rate of μ_c repairs/year as seen in Fig. 3.2(a).

2. Repairing the system when the capacitor is at 0.935 of its nominal value, i.e., repairing the capacitor when the system reaches state 5 and state 7, at a rate of μ_c repairs/year as seen in Fig. 3.2(b).

3. Repairing the system every time the capacitor degrades, i.e., repairing the capacitor when the system reaches state 3, 5 and 7, at a rate of μ_c repairs/year as seen in Fig. 3.2(c).

To determine the availability at time t, we solve the Chapman-Kolmogorov equation, updating the state transition matrix for every repair strategy.

3.2.2 Architecture 2

This architecture uses the same repair strategies but with updated repair rates to account for the change in the architecture, i.e., the addition of 24 diodes, six active switches. The repair rate μ_{ar} now accounts for the repairs of components in the active and passive rectifiers as well as the auxiliary components. Repair rate μ_c is reduced by half because of the addition of a capacitor.

3.2.3 Architecture 3

Changes were made to the different repair strategies because failures in the passive rectifier do not result in a system failure. A characteristic that both repair strategies share is that repair is possible from states where the failure has occurred due to switches or auxiliary components, i.e., when the system is in transition from state 13 to 1, 14 to 4, 15 to 7, 16 to 10, 17 to 2, 18 to 5, 19 to 8, 20 to 11, 21 to 3, 22 to 6, 23 to 9 and 24 to 12 at a rate of μ_{ar} repairs/year as seen in Fig. 3.3. The impact of the capacitor-focused repair strategies on the availability of the architecture will not be studied as it is covered extensively in Sections 3.2.1 and 3.2.2. Therefore, the capacitor will only be repaired when degradation has reached 0.895 of its nominal capacitance, i.e., a transition from state 25 to 1, 26 to 4, 27 to 7 and 28 to 10 at a rate of μ_c repairs/year. Repair rates for the passive rectifiers, μ_{pr1}, μ_{pr2}, and μ_{pr3} are included. The following repair strategies are considered:

1. Repairing the system, one passive rectifier at a time, i.e., if three passive rectifiers fail, repair one at the rate of μ_{pr1}, then the next passive rectifier at the same rate, μ_{pr1} and so on, as seen in Fig. 3.3(a). Note that this only works if the system can be repaired while it is still in operation.

2. Repairing the system all at once when any passive rectifier fails, i.e., if one, two or three passive rectifiers fail, the system is shut down and all the failed passive rectifiers are fixed at a rate of μ_{pr1} for one passive rectifier, rate of μ_{pr2} for two passive rectifiers, and rate of μ_{pr3} for three passive rectifiers, as seen in Fig. 3.3(b).

The Chapman-Kolmogorov equation is solved to determine availability at time t, updating the state transition matrix for both repair strategies.

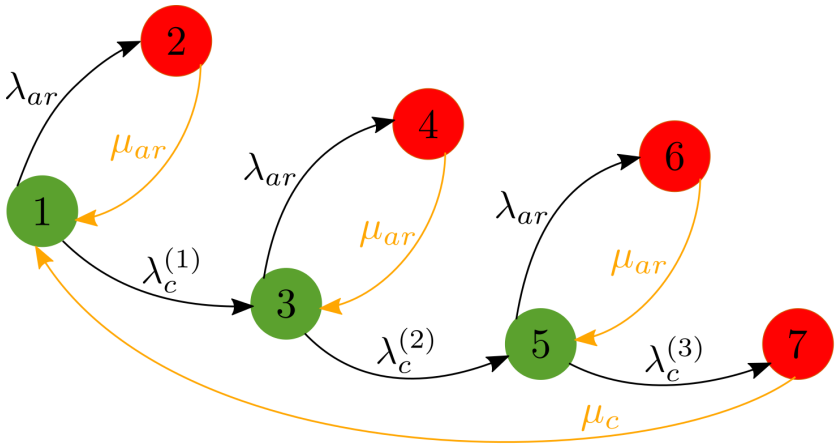

(a)

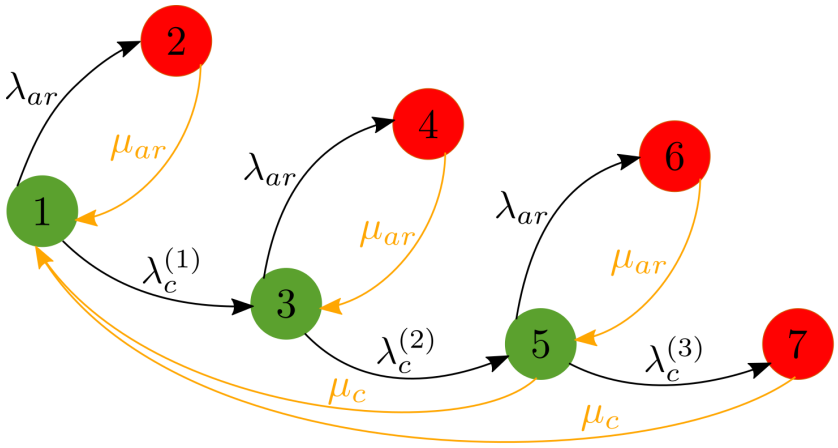

(b)

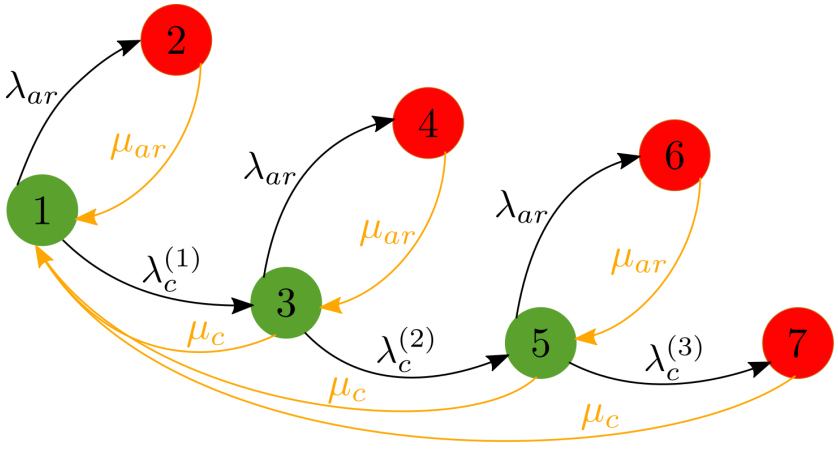

(c)

Figure 3.2: Markov availability model state-transition diagram for Architectures 1 and 2 for (a) repair strategy 1, (b) 2, and (c) 3.

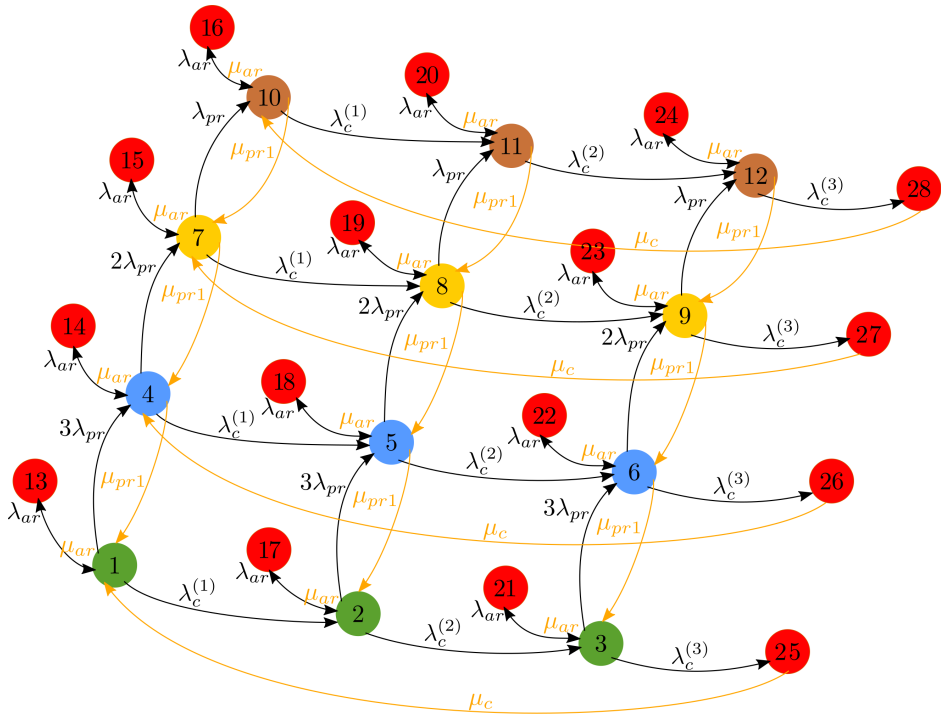

(a)

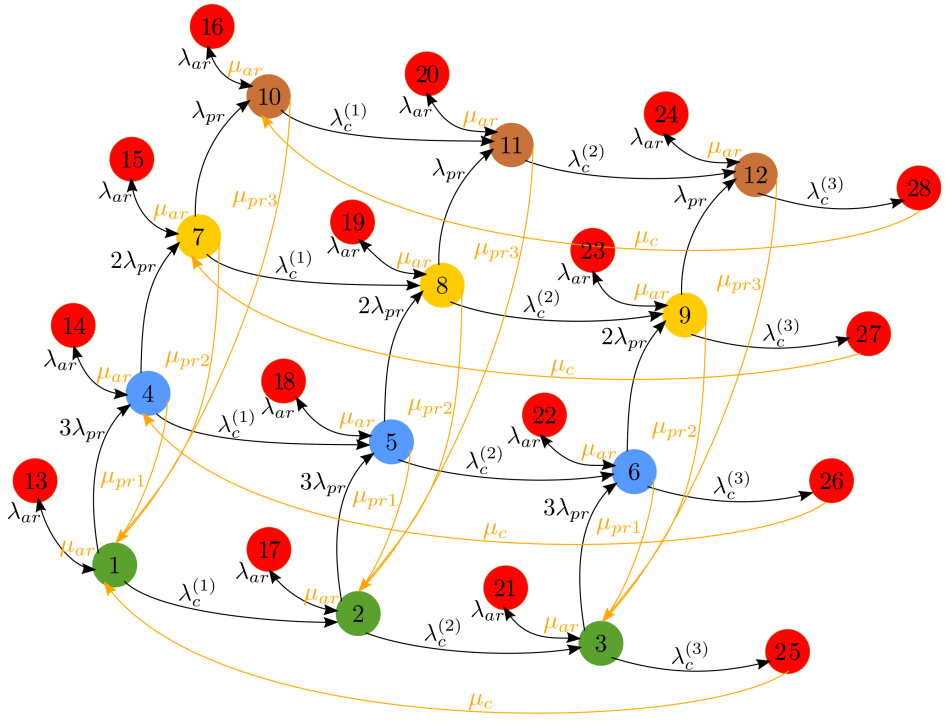

(b)

Figure 3.3: Markov availability model state-transition diagram for Architecture 3 for repair strategy (a) 1 and (b) 2.

3.3 Numerical Results

The values in Table 3.1, calculated using information from [31] and [32], are in units of repairs/year. The repair rates were calculated using repair times for different sub-assemblies/components of off-shore wind turbines and weighting them differently to accommodate for the increase in number of components for the different converter architectures. All the availability calculations in this section are done for $t = 30$ years.

Table 3.1: Repair Rates

Repair Rates	Architecture 1	Architecture 2	Architecture 3
μ_c	87.6	43.8	43.8
μ_{ar}	649.16	n/a	336.96
μ_e	n/a	160.12	n/a
μ_{pr1}	n/a	n/a	739.93
μ_{pr2}	n/a	n/a	369.97
μ_{pr3}	n/a	n/a	246.64

Regardless of the different repair strategies simulated, Architecture 1 has lower availability than Architecture 2 as seen in Table 3.2. There is insignificant change in availability between the different repair strategies for Architecture 2 but an order of magnitude change for Architecture 1 between repair strategies 1 and 2, an increase of 0.1% which Fig. 3.4 confirms. This shows that Architecture 2 is not just more available but also more robust with respect to different repair strategies. The availability graph of the Architecture 2 is not shown as their lines overlap.

Table 3.3 shows there are no noticeable differences in the availability of Architecture 3 with respect to the different repair strategies simulated. The power produced also shows no noticeable differences with respect to the different repair strategies simulated. The availability and power-produced graphs of Architecture 3 are not shown as their lines overlap.

Table 3.2: Availability

Repair Strategies	Architecture 1	Architecture 2
1	0.9981	0.9995
2	0.9991	0.9995
3	0.9991	0.9995

Table 3.3: Availability of Architecture 3

Repair Strategies	Availability	Power Produced [p.u.]
1	0.9998	0.9998
2	0.9998	0.9998

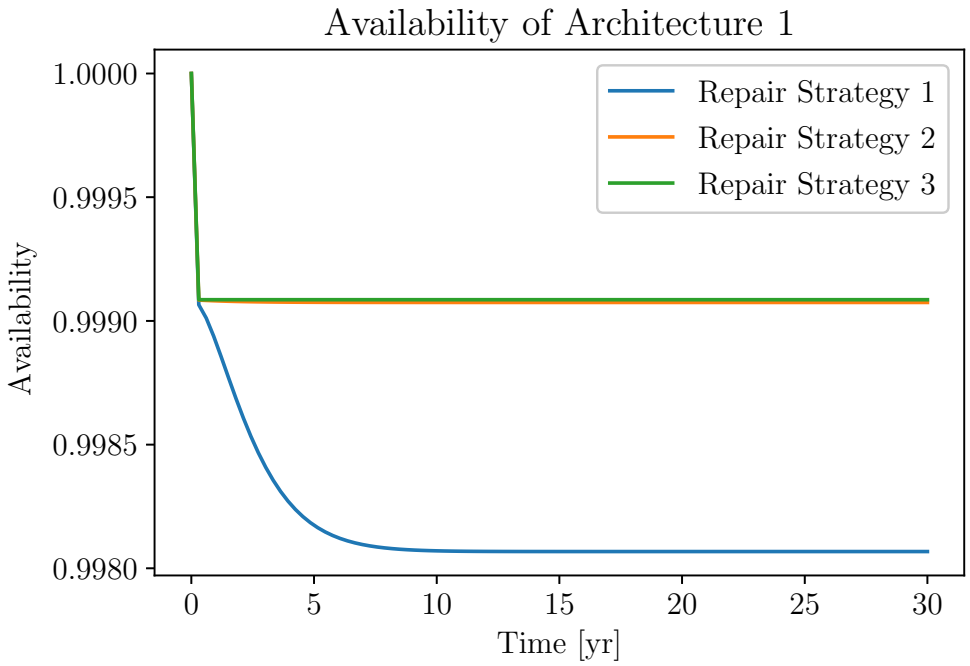

Figure 3.4: Availability of Architecture 1 over time for repair strategies 1, 2, and 3.

3.4 Sensitivity Analysis

For the Markov availability model, sensitivity analysis is done on the availability (and power produced for Architecture 3) of each converter architecture, by first scaling the failure rate under investigation by κ, while holding all other failure and repair rates constant, κ ranging from 1 to 10. Then, the same Chapman-Kolmogorov equation discussed in Section 2.1 is used to calculate the availability. This process is done for the following failure rates: λ_{as}, $\lambda_c^{(1)}$, $\lambda_c^{(2)}$, $\lambda_c^{(3)}$, and λ_d. This process is then repeated for repair rates μ_{pr1}, μ_{pr2} and μ_{pr3}, with χ, the repair rate multiplier which ranges from 1 to 10^{-3}. We can then compare the impact of the scaled failure and repair rates on the availability and power produced of the different converter architectures.

3.4.1 Architecture 1

Figure 3.5(a) shows that availability of Architecture 1 is much more affected by λ_{as} and $\lambda_c^{(1)}$ than the other failure rates, although all the capacitor-failure-rates effects on the availability result in asymptotes around 1, while the active-switches failure rate sends availability to zero. The largest reduction in availability by the failure rates is 0.18%. For the repair rates, as seen in Fig. 3.5(b), μ_{ar} and μ_c have similar effects in repair strategy 1. Reducing the repair rates by a magnitude of 10 does not significantly impact the availability.

Repair strategies 2 and 3 have similar plots, hence only Fig. 3.6(a) is shown. The failure rates of the capacitor have negligible effects on the converter architecture's availability but the effect of λ_{as} is more pronounced, reducing the availability by 0.18% scaling λ_{as} by 10. These repair strategies, however, allow for a higher availability than repair strategy 1 as seen in Table 3.2. As for repair rates, as seen in Fig. 3.6(b), μ_{ar} has a little more effect on the availability than μ_c, because μ_c is used many more times in these repair strategies.

3.4.2 Architecture 2

The sensitivity of the availability of Architecture 2 with respect to the three different repair strategies is essentially the same because of the reduced failure rates of the capacitor; hence only the results for repair strategy 3 are shown in this thesis. Figure 3.7(a) shows information similar to Fig. 2.7, that diodes have significant effect on the availability (a reduction of 0.17%) and active switches are next, although their effects are a lot less. As seen in Fig. 3.7(b), because the capacitors now have reduced failure rates, a scale reduction of 10^{-3} in μ_c results in negligible change in the availability compared to μ_e, which reduces the availability by 0.35 with the same scale reduction. Note that the drop in availability is still better in Architecture 2 than in Architecture 1 as seen in Figs. 3.5(b) and 3.6(b).

3.4.3 Architecture 3

There are no significant differences in sensitivity of availability or power produced of Architecture 3 when comparing the two repair strategies, when the values are scaled with magnitudes of 10 for the failure rates and 10^{-3} for repair rates as seen in Fig. 3.8. Hence the rest of the graphs are not shown in this thesis. With this information, neither repair strategy is recommended over the other as both have similar results.

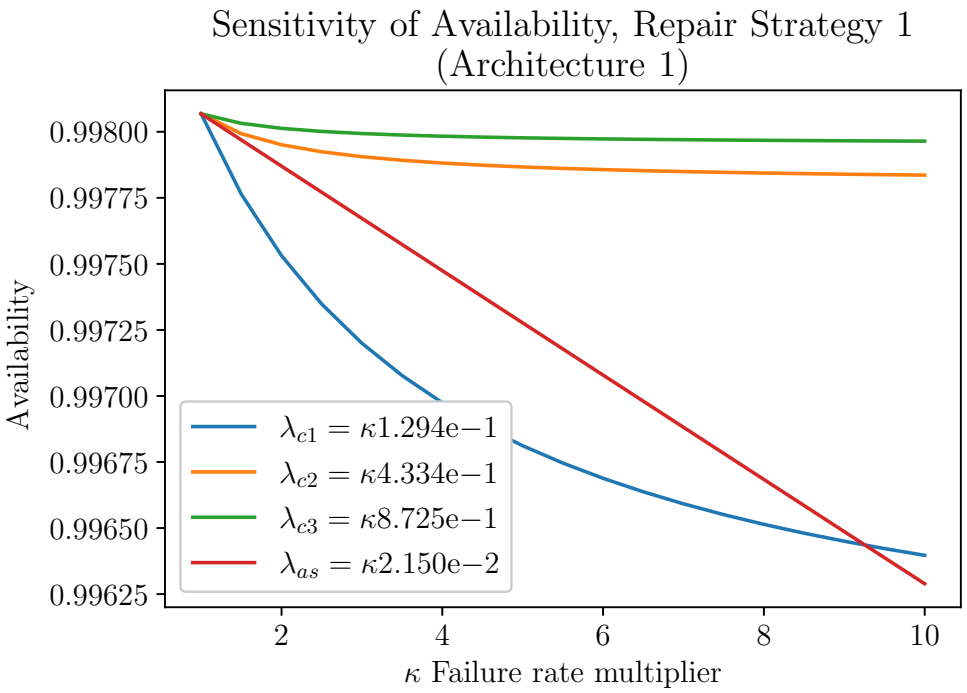

(a)

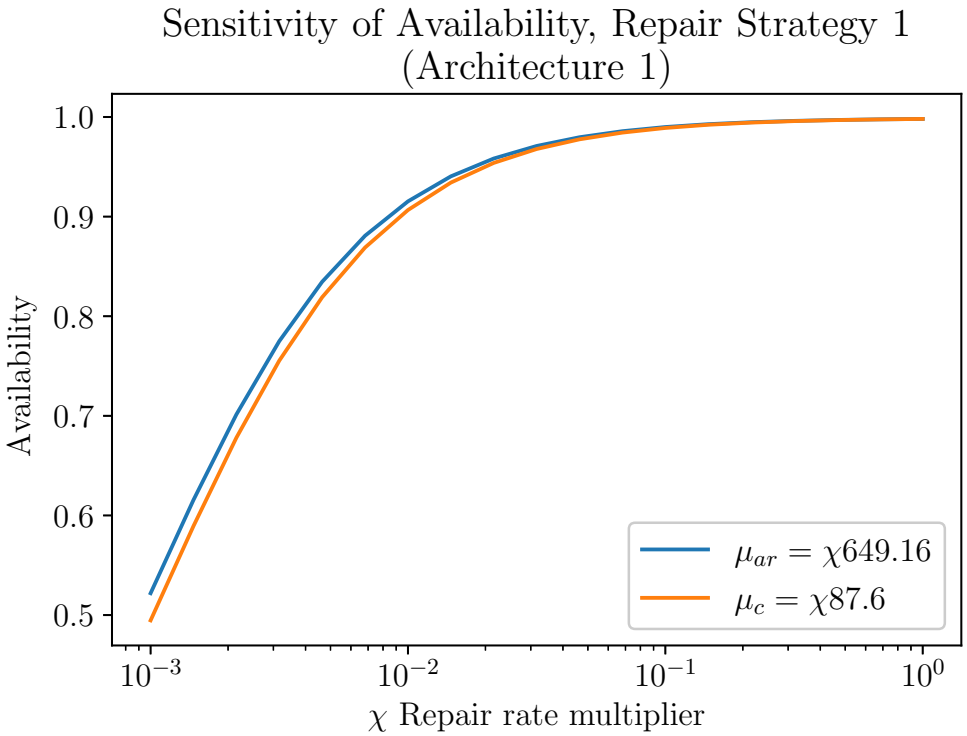

(b)

Figure 3.5: Sensitivity of availability for Architecture 1 with respect to varying (a) failure rates and (b) repair rates at $t = 30$ years for repair strategy 1.

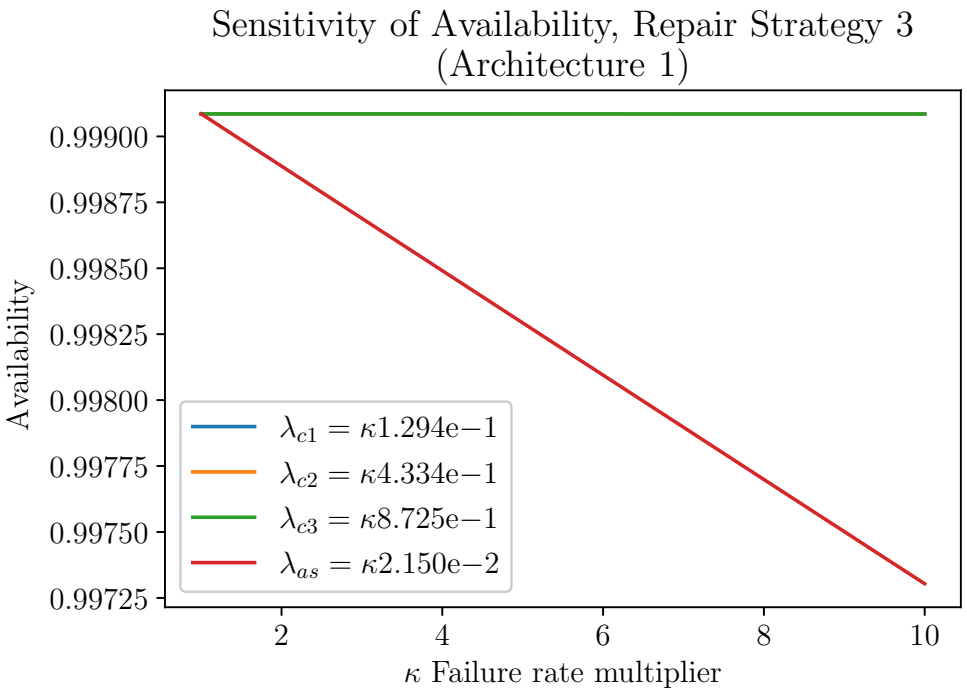

(a)

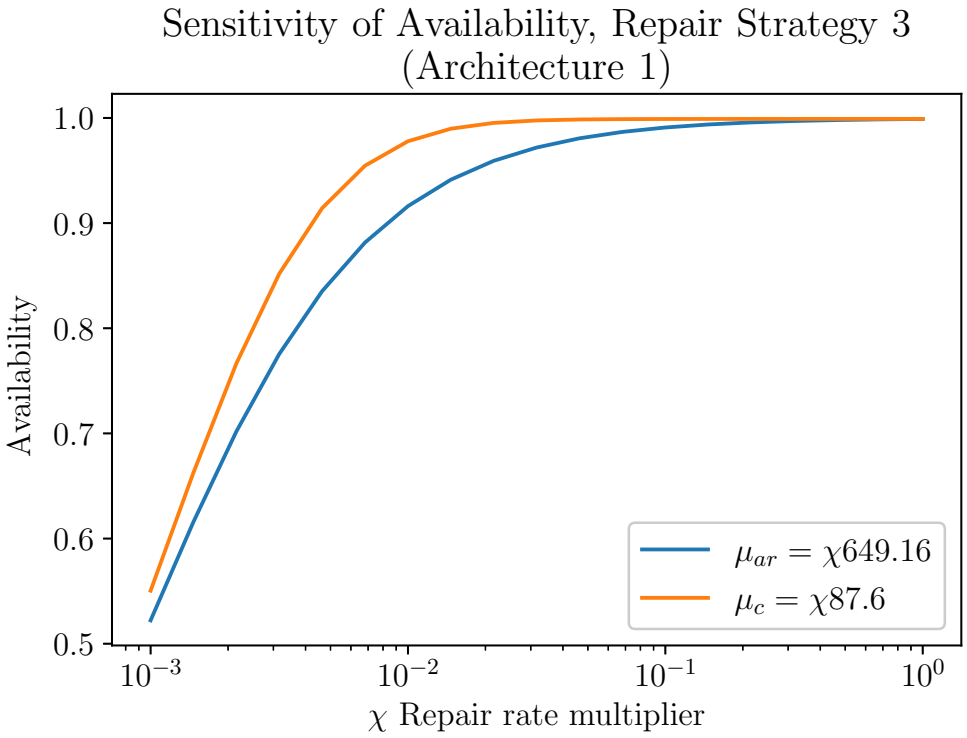

(b)

Figure 3.6: Sensitivity of availability for Architecture 1 with respect to varying (a) failure rates and (b) repair rates at $t = 30$ years for repair strategy 3.

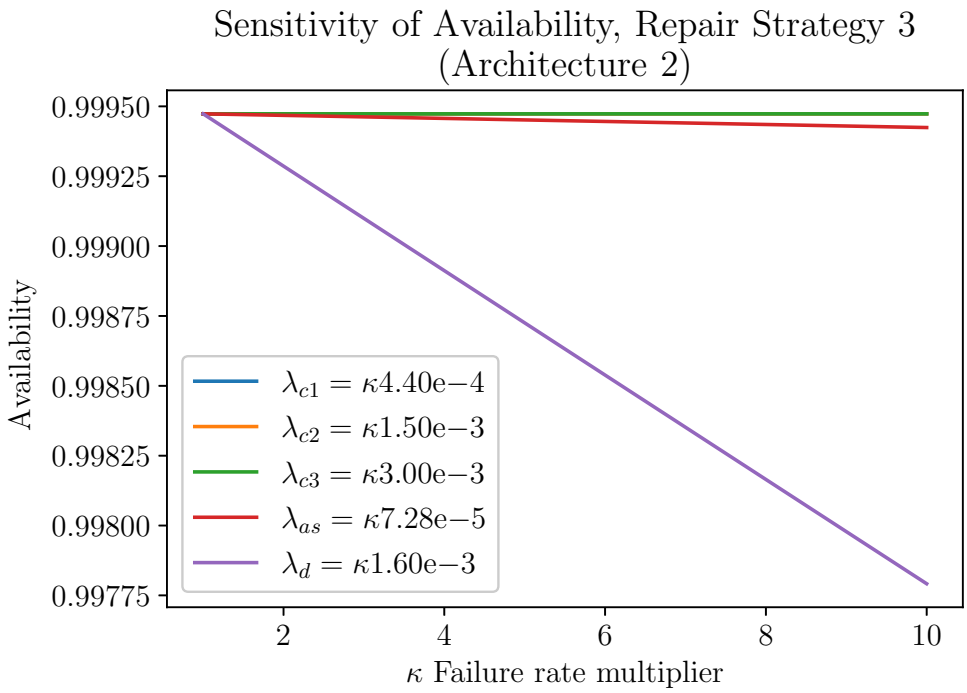

(a)

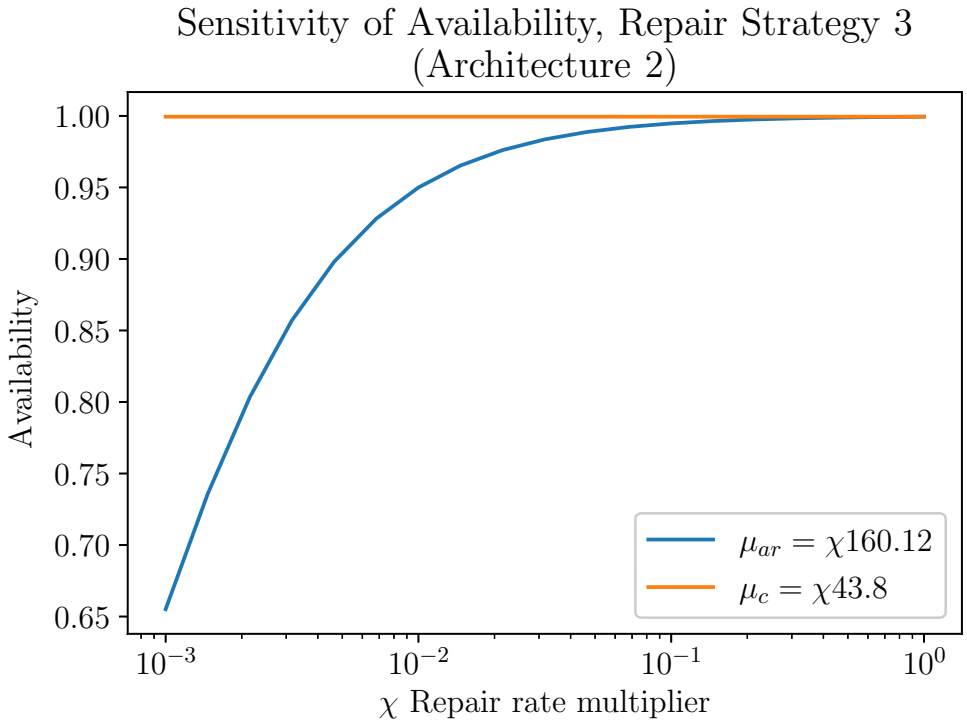

(b)

Figure 3.7: Sensitivity of availability for Architecture 2 with respect to varying (a) failure rates and (b) repair rates at $t = 30$ years for repair strategy 3.

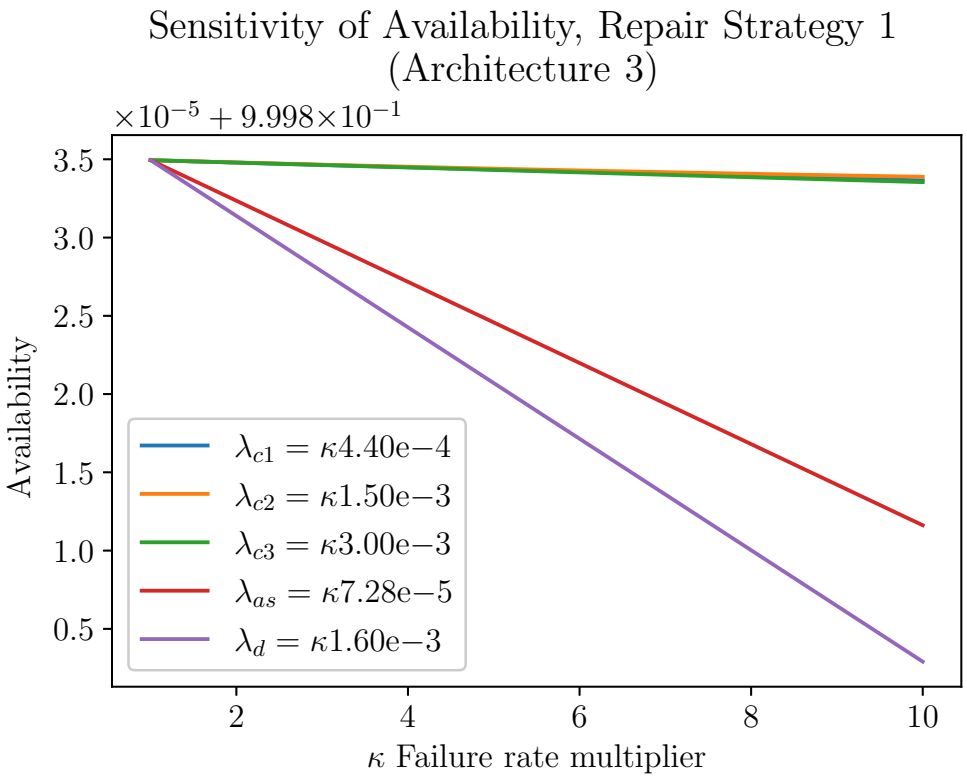

(a)

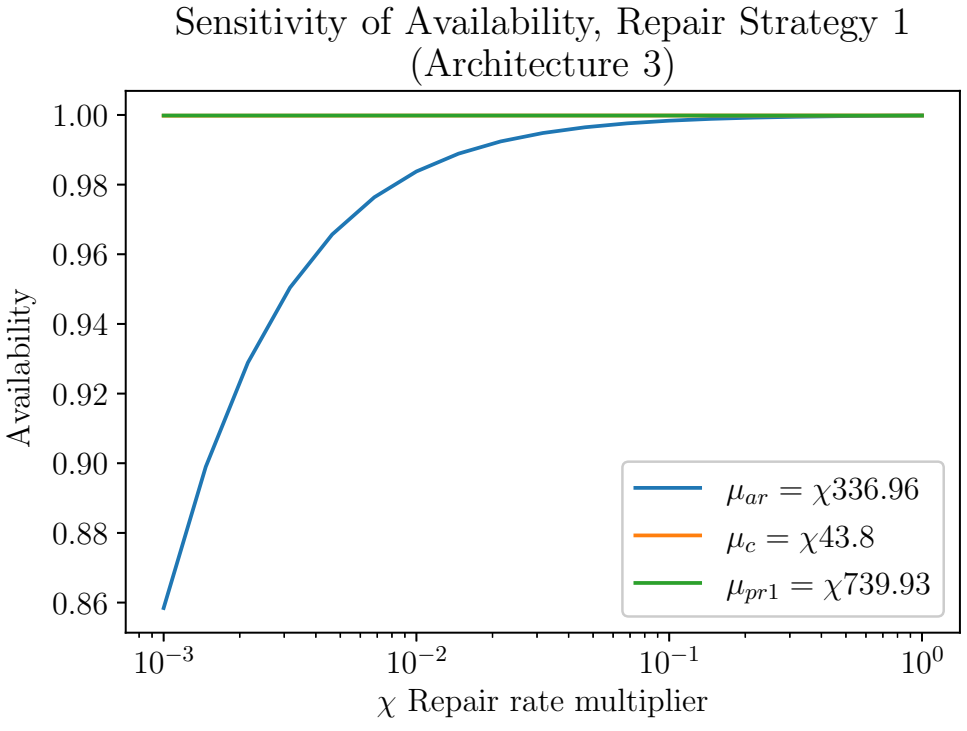

(b)

Figure 3.8: Sensitivity of availability for Architecture 3 with respect to varying failure rates at $t = 30$ years for repair strategy 1.

CHAPTER 4

MODEL-ORDER REDUCTION

Model-order reduction is a powerful tool used to reduce the complexity of a set of differential equations to enhance computation speed while maintaining high accuracy. Singular perturbation analysis, the technique used in this work for model-order reduction, looks to separate the fast-varying states from the slow-varying states and reduce the behavior of the fast-varying states to an algebraic set of equations, reducing the order of the model.

4.1 Averaged High-Order Model

In this section, we present the averaged high-order dynamical model for a wind turbine using integrated generator–rectifier systems covering control- and physical-layer subsystems [18].

4.1.1 Passive Rectifier Equations

Consider a PMSG with k three-phase ac ports, $(k-1)$ of which power passive rectifiers with no output filter capacitors. Assuming a constant dc-bus current I_{dc} and a negligible voltage ripple, the total dc output voltage of the $(k-1)$ passive rectifiers at the electrical frequency ω is

$$V_p = \frac{3}{\pi}(k-1)\sqrt{3}E(\omega) - (k-1)\left(\frac{3}{\pi}\omega L + 2R\right)I_{dc}, \tag{4.1}$$

where L is the synchronous inductance and R is the per-phase equivalent series resistance of each ac port [33]. $E(\omega)$, the back EMF, is electrical-frequency-dependent as seen below:

$$E(\omega) = \frac{\omega}{2\pi f_0} E_0, \tag{4.2}$$

where f_0 is the rated electrical frequency and E_0 is the rated line-to-neutral peak back EMF of each ac port.

4.1.2 Active Rectifier Equations

Using KCL, the relationship between the dc-bus current, I_{dc} , the total current going into the active rectifier, I_l, and the ripple current flowing through the capacitor, I_{cap}, is as follows:

$$I_l = I_{cap} + I_{dc}, \tag{4.3}$$

$$I_{cap} = C\frac{dV_a}{dt}, \tag{4.4}$$

where V_a is the active-rectifier dc-side voltage and C is the capacitance of the capacitor in the active rectifier. The power balance between the ac and the dc sides of the active rectifier is

$$V_a I_l = \frac{3}{2} E(\omega) I_{sd} - \frac{3}{2} I_{sd}^2 R, \tag{4.5}$$

where I_{sd} is the d-axis component of the active-rectifier ac-side current. V_a, the active-rectifier dc-side voltage is given by

$$V_a = V_{dc} - V_p, \tag{4.6}$$

where V_{dc} is the constant grid interface voltage. V_{dc}, along with P_{dc}, the dc-bus power, is used to determine the dc-bus current,

$$I_{dc} = \frac{P_{dc}}{V_{dc}}. \tag{4.7}$$

4.1.3 Control Architecture Equations

Power-flow control is achieved by using inner loop current controllers that regulate the d-axis and q-axis currents of the active rectifier and an outer loop power controller that calculates the reference input dc-bus power, P^*_{dc}. The d-axis is aligned with the peak phase-A back EMF. The q-axis leads the d-axis by 90^{circ}. The current controllers are designed based on the ac-port current dynamics in the dq reference frame given by the following equations:

$$L\frac{dI_{sd}}{dt} = -RI_{sd} + \omega LI_{sq} + E(\omega) - V_{rd}, \tag{4.8}$$

$$L\frac{dI_{sq}}{dt} = -RI_{sq} - \omega LI_{sd} - V_{rq}, \tag{4.9}$$

where I_{sq} is the q-axis component of the active-rectifier ac-side current, and V_{rd} and V_{rq} are the input d-axis and q-axis voltages, respectively. A PI controller with feed-forward terms is chosen to produce the d-axis voltage command,

$$V_{rd} = k_{\mathrm{p}i}\frac{d\xi_d}{dt} + k_{\mathrm{i}i}\xi_d + E(\omega) + \omega LI_{sq}, \tag{4.10}$$

$$\frac{d\xi_d}{dt} = I^*_{sd} - I_{sd}, \tag{4.11}$$

where I^*_{sd} is the reference input d-axis current, $k_{\mathrm{p}i}$ and $k_{\mathrm{i}i}$ are the proportional and integral gains respectively, and ξ_d is integral of the difference between the reference and input d-axis currents. The same is done for the q-axis controller with ξ_q being introduced, except that I^*_{sq} is set to zero; this results in

$$V_{rq} = k_{\mathrm{p}i}\frac{d\xi_q}{dt} + k_{\mathrm{i}i}\xi_q - \omega LI_{sd}, \tag{4.12}$$

$$\frac{d\xi_q}{dt} = -I_{sq}. \tag{4.13}$$

Outer-loop PI control is given by

$$I_{sd}^{*} = k_{\text{pp}}\frac{d\sigma}{dt} + k_{\text{ip}}\sigma, \tag{4.14}$$

$$\frac{d\sigma}{dt} = P_{dc}^{*} - P_{dc}, \tag{4.15}$$

where σ is the integral of the difference between the reference and input dc-bus power. The proposed power-control architecture is applied to track the wind turbine maximum power point. Maximum power point tracking (MPPT) is achieved if at each generator speed, the electrical power drawn follows the maximum power curve from [34]; this condition is captured by the following relation

$$P_{dc}^{*} = \begin{cases} \frac{S}{(2\pi f_0)^3}\omega^3, & \omega \leq 2\pi f_0, \\ \\ S, & \omega > 2\pi f_0. \end{cases}$$

4.1.4 Mechanical Equations

The reference speed to the generator is the rotational speed ω_m of a wind turbine with dynamics

$$J\omega_m\frac{d\omega_m}{dt} = P_t - P_{dc}, \tag{4.16}$$

$$\omega_m = \frac{2}{p}\omega, \tag{4.17}$$

where J is the wind-turbine moment of inertia and p is the number of poles in the generator. The turbine power, P_t, is determined by

$$P_t = \frac{1}{2}\rho A\nu^3 C_p, \tag{4.18}$$

where ν is the wind speed, ρ is the air density, A is the swept area of the wind turbine blades, and C_p is the efficiency of the wind turbine. C_p is a function of the tip speed ratio, λ, the value of which can be determined by [35]:

$$\lambda(\omega) = \frac{2R_{blade}\omega}{p\nu}. \tag{4.19}$$

4.1.5 State Space Model

The equations in sections 4.1.1–4.1.4 are used to derive the following state space model.

$$\begin{aligned}\frac{dV_a}{dt} &= \frac{3E_0\omega}{4C\pi f_0}\frac{I_{sd}}{V_a} - \frac{3R}{2C}\frac{I_{sd}^2}{V_a} \\ &\quad - \frac{1}{C\left(\frac{3}{\pi}L\omega + 2R\right)}\left(\frac{V_a}{(k-1)} - \frac{V_{dc}}{(k-1)} + \frac{3\sqrt{3}E_0\omega}{2\pi^2 f_0}\right),\end{aligned} \tag{4.20}$$

$$\begin{aligned}\frac{dI_{sd}}{dt} &= -\frac{R}{L}I_{sd} + \frac{k_{\mathrm{p}i}}{L}I_{sd} - \frac{k_{\mathrm{i}i}}{L}\xi_d - \frac{k_{\mathrm{p}i}k_{\mathrm{i}p}}{L}\sigma - \frac{Sk_{\mathrm{p}i}k_{\mathrm{p}p}}{(2\pi f_0)^3 L}\omega^3 \\ &\quad + \frac{k_{\mathrm{p}i}k_{\mathrm{p}p}V_{dc}}{L\left(\frac{3}{\pi}L\omega + 2R\right)}\left(\frac{V_a}{(k-1)} - \frac{V_{dc}}{(k-1)} + \frac{3\sqrt{3}E_0\omega}{2\pi^2 f_0}\right),\end{aligned} \tag{4.21}$$

$$\frac{dI_{sq}}{dt} = -\frac{R}{L}I_{sq} + \frac{k_{\mathrm{p}i}}{L}I_{sq} - \frac{k_{\mathrm{i}i}}{L}\xi_q, \tag{4.22}$$

$$\begin{aligned}\frac{d\omega}{dt} &= \frac{\rho A C_p \nu^3 p^2}{8J\omega} \\ &\quad - \frac{V_{dc}p^2}{4J\omega\left(\frac{3}{\pi}L\omega + 2R\right)}\left(\frac{V_a}{(k-1)} - \frac{V_{dc}}{(k-1)} + \frac{3\sqrt{3}E_0\omega}{2\pi^2 f_0}\right),\end{aligned} \tag{4.23}$$

$$\begin{aligned}\frac{d\xi_d}{dt} &= k_{\mathrm{i}p}\sigma - I_{sd} + \frac{Sk_{\mathrm{p}p}}{(2\pi f_0)^3}\omega^3 \\ &\quad - \frac{k_{\mathrm{p}p}V_{dc}}{\left(\frac{3}{\pi}L\omega + 2R\right)}\left(\frac{V_a}{(k-1)} - \frac{V_{dc}}{(k-1)} + \frac{3\sqrt{3}E_0\omega}{2\pi^2 f_0}\right),\end{aligned} \tag{4.24}$$

$$\frac{d\xi_q}{dt} = -I_{sq}, \tag{4.25}$$

$$\begin{aligned}\frac{d\sigma}{dt} &= \frac{S}{(2\pi f_0)^3}\omega^3 \\ &\quad - \frac{V_{dc}}{\left(\frac{3}{\pi}L\omega + 2R\right)}\left(\frac{V_a}{(k-1)} - \frac{V_{dc}}{(k-1)} + \frac{3\sqrt{3}E_0\omega}{2\pi^2 f_0}\right).\end{aligned} \tag{4.26}$$

4.2 Reduced-Order Model

In this section, we present the reduced-order model for the wind turbine using integrated generator rectifier systems. The fast and slow states in the dynamic model of the wind energy conversion system were identified using their participation factors and eigenvalues based on singular perturbation analysis [36].

For the linear system $\dot{x} = Gx$, where $G \in \mathbb{R}^{n\times n}$, $x \in \mathbb{R}^n$, let r_{ij} and l_{ij} be the i-th entries of the right and left eigenvectors associated with the j-th eigenvalue of G, respectively. As seen in [37], the participation factor of the i-th element of x in the j-th eigenvalue of A is given by

$$\frac{\left|r_{ij}\right|\left|l_{ij}\right|}{\sum_{i=1}^{n}\left|r_{ij}\right|\left|l_{ij}\right|}. \tag{4.27}$$

The participation factors are then normalized using their maximum values. The identification of the fast and slow states is done by plotting the eigenvalues and participation factors corresponding to a linearized version of the wind turbine using integrated generator-rectifier systems with the parameters and initial conditions presented in Tables 4.1 and 4.2, respectively.

Using Fig. 4.1, we can determine that a bandwidth of 5 rads^{-1} is reasonable to separate slow and fast varying states. The cutoff bandwidth is selected by determining the desired order of the reduced-order model (2nd) and selecting a bandwidth based on the number of eigenvalues of the right of the cut-off. Singular perturbation analysis is used to complete the model-order reduction. To this end, we need to assume the following holds:

$$\left|\frac{\omega-\omega_0}{\omega_0}\right| \leq \epsilon, \tag{4.28}$$

where ϵ is a dimensionless parameter. For nominal frequency, $\omega_0 = 2\pi f_0$ rad/s, ϵ is chosen to be 5^{-1} because of the cutoff bandwidth. Therefore, this assumption implies that the reduced-order model is valid when ω is within 100.53 and 150.80 rad/s.

The right- and left-hand sides of the differential equations of the averaged high-order model for the fast states are multiplied by $\epsilon = 5^{-1}$. The resulting equations are in standard singular perturbation form:

$$\frac{dx}{dt} = f(x, z, \epsilon), \tag{4.29}$$

$$\epsilon\frac{dz}{dt} = g(x, z, \epsilon), \tag{4.30}$$

where $f(x, z, \epsilon)$ and $g(x, z, \epsilon)$ are continuously differentiable functions of their arguments, the elements of x are the slow-varying states, ω, and σ, and the elements of z are the fast-varying states, V_a, I_{sd}, I_{sq}, ξ_d, and ξ_q. The set of differential equations constituting (4.30) are replaced with algebraic equations that are determined by setting $\epsilon = 0$ on the left-hand side of (4.30), $\left|\frac{\omega-\omega_0}{\omega_0}\right| = 0$ in the resulting set of equations and solving for z as a function of x. This results in a seventh-order model being reduced to a second-order model for the wind turbine using integrated generator-rectifier system.

The dynamics of the slow-varying states are given below:

$$\begin{aligned}\frac{d\omega}{dt} &= \frac{\rho A C_p \nu^3 p^2}{8J\omega} \\ &\quad - \frac{V_{dc}p^2}{4J\omega\left(\frac{3}{\pi}L\omega + 2R\right)}\left(\frac{V_a}{(k-1)} - \frac{V_{dc}}{(k-1)} + \frac{3\sqrt{3}E_0\omega}{2\pi^2 f_0}\right),\end{aligned} \tag{4.31}$$

$$\begin{aligned}\frac{d\sigma}{dt} &= \frac{S}{(2\pi f_0)^3}\omega^3 \\ &\quad - \frac{V_{dc}}{\left(\frac{3}{\pi}L\omega + 2R\right)}\left(\frac{V_a}{(k-1)} - \frac{V_{dc}}{(k-1)} + \frac{3\sqrt{3}E_0\omega}{2\pi^2 f_0}\right).\end{aligned} \tag{4.32}$$

The fast-varying states are calculated with the following algebraic equations:

$$\begin{aligned} I_{sd} = {} & k_{\mathrm{ip}}\sigma + \frac{Sk_{\mathrm{pp}}}{(2\pi f_0)^3}\omega^3 \\ & - \frac{k_{\mathrm{pp}}V_{dc}}{\left(\frac{3}{\pi}L\omega + 2R\right)}\left(\frac{3\sqrt{3}E_0\omega}{2\pi^2 f_0} - \frac{V_{dc}}{(k-1)}\right) \\ & - \frac{k_{\mathrm{pp}}V_{dc}V_a}{(k-1)\left(\frac{3}{\pi}L\omega + 2R\right)}, \end{aligned} \tag{4.33}$$

$$I_{sq} = 0, \tag{4.34}$$

$$\begin{aligned} \xi_d = {} & -\frac{R}{k_{\mathrm{ii}}}I_{sd} + \frac{k_{\mathrm{pi}}}{k_{\mathrm{ii}}}I_{sd} - \frac{k_{\mathrm{pi}}k_{\mathrm{ip}}}{k_{\mathrm{ii}}}\sigma - \frac{Sk_{\mathrm{pi}}k_{\mathrm{pp}}}{(2\pi f_0)^3 k_{\mathrm{ii}}}\omega^3 \\ & + \frac{k_{\mathrm{pi}}k_{\mathrm{pp}}V_{dc}}{k_{\mathrm{ii}}\left(\frac{3}{\pi}L\omega + 2R\right)}\left(\frac{V_a}{(k-1)} - \frac{V_{dc}}{(k-1)} + \frac{3\sqrt{3}E_0\omega}{2\pi^2 f_0}\right), \end{aligned} \tag{4.35}$$

$$\xi_q = 0, \tag{4.36}$$

$$V_a = \frac{-b - \sqrt{b^2 - 4ac}}{2a}, \tag{4.37}$$

where

$$\begin{aligned} a = {} & -\frac{3R}{2C}\left(\frac{k_{\mathrm{pp}}V_{dc}}{(k-1)\left(\frac{3}{\pi}L\omega + 2R\right)}\right)^2 \\ & - \frac{1}{C(k-1)\left(\frac{3}{\pi}L\omega + 2R\right)}, \end{aligned} \tag{4.38}$$

$$\begin{aligned} b = {} & -\Bigg(\frac{3E_0\omega}{4C\pi f_0}\frac{k_{\mathrm{pp}}V_{dc}}{(k-1)\left(\frac{3}{\pi}L\omega + 2R\right)} \\ & + \frac{1}{C\left(\frac{3}{\pi}L\omega + 2R\right)}\left(\frac{3\sqrt{3}E_0\omega}{2\pi^2 f_0} - \frac{V_{dc}}{(k-1)}\right) \\ & + \frac{3R}{2C}\Bigg(- \frac{2k_{\mathrm{ip}}k_{\mathrm{pp}}V_{dc}\sigma}{(k-1)\left(\frac{3}{\pi}L\omega + 2R\right)} \end{aligned}$$

$$
\begin{aligned}
&- \frac{2k_{\mathrm{pp}}V_{dc}}{(k-1)\left(\frac{3}{\pi}L\omega+2R\right)}\left(\frac{Sk_{\mathrm{pp}}\omega^3}{(2\pi f_0)^3}\right)\\
&+ \frac{2(k_{\mathrm{pp}}V_{dc})^2}{(k-1)\left(\frac{3}{\pi}L\omega+2R\right)^2}\left(\frac{3\sqrt{3}E_0\omega}{2\pi^2 f_0}-\frac{V_{dc}}{(k-1)}\right)\Bigg)\Bigg),
\end{aligned}
\tag{4.39}
$$

$$
\begin{aligned}
c = \frac{3E_0\omega}{4C\pi f_0}\Bigg(&k_{\mathrm{ip}}\sigma+\frac{Sk_{\mathrm{pp}}}{(2\pi f_0)^3}\omega^3\\
&- \frac{k_{\mathrm{pp}}V_{dc}}{\left(\frac{3}{\pi}L\omega+2R\right)}\left(\frac{3\sqrt{3}E_0\omega}{2\pi^2 f_0}-\frac{V_{dc}}{(k-1)}\right)\Bigg)\\
&- \frac{3R}{2C}\Bigg(\left(k_{\mathrm{ip}}\sigma\right)^2+\frac{2Sk_{\mathrm{pp}}k_{\mathrm{ip}}\sigma\omega^3}{(2\pi f_0)^3}\\
&- \frac{2k_{\mathrm{ip}}k_{\mathrm{pp}}V_{dc}\sigma}{\left(\frac{3}{\pi}L\omega+2R\right)}\left(\frac{3\sqrt{3}E_0\omega}{2\pi^2 f_0}-\frac{V_{dc}}{(k-1)}\right)\\
&+ \left(\frac{Sk_{\mathrm{pp}}\omega^3}{(2\pi f_0)^3}\right)^2-\frac{2k_{\mathrm{pp}}V_{dc}}{\left(\frac{3}{\pi}L\omega+2R\right)}\left(\frac{Sk_{\mathrm{pp}}\omega^3}{(2\pi f_0)^3}\right)\left(\frac{3\sqrt{3}E_0\omega}{2\pi^2 f_0}\right.\\
&\left.- \frac{V_{dc}}{(k-1)}\right)+\left(\frac{k_{\mathrm{pp}}V_{dc}}{\left(\frac{3}{\pi}L\omega+2R\right)}\left(\frac{3\sqrt{3}E_0\omega}{2\pi^2 f_0}-\frac{V_{dc}}{(k-1)}\right)\right)^2\Bigg).
\end{aligned}
\tag{4.40}
$$

4.3 Numerical Results

The averaged high-order model and the reduced-order model are built in MATLAB Simulink. Their input is a normally distributed random signal with mean 11, variance 0.5, seed 1 and sample time 1. The elapsed time to run the averaged high-order model and the reduced-order model is 55.44 s and 16.75 s, respectively. The reduced-order model runs with simulation time one third that of the averaged high-order model, a significant decrease in computational effort. If outputs for the fast states are not calculated and displayed, the simulation time is 1.12 s. As seen in Fig. 4.2, the root mean square error (RMSE) of the reduced-order model relative to the averaged high-order model, amongst all states, is below 10^{-2}. Note that the RMSE is calculated with the state variables in per unit based on their rated values. Figure 4.3 shows that the reduced-order model displays the transient behavior of the state variables just as the averaged high-order model does with high

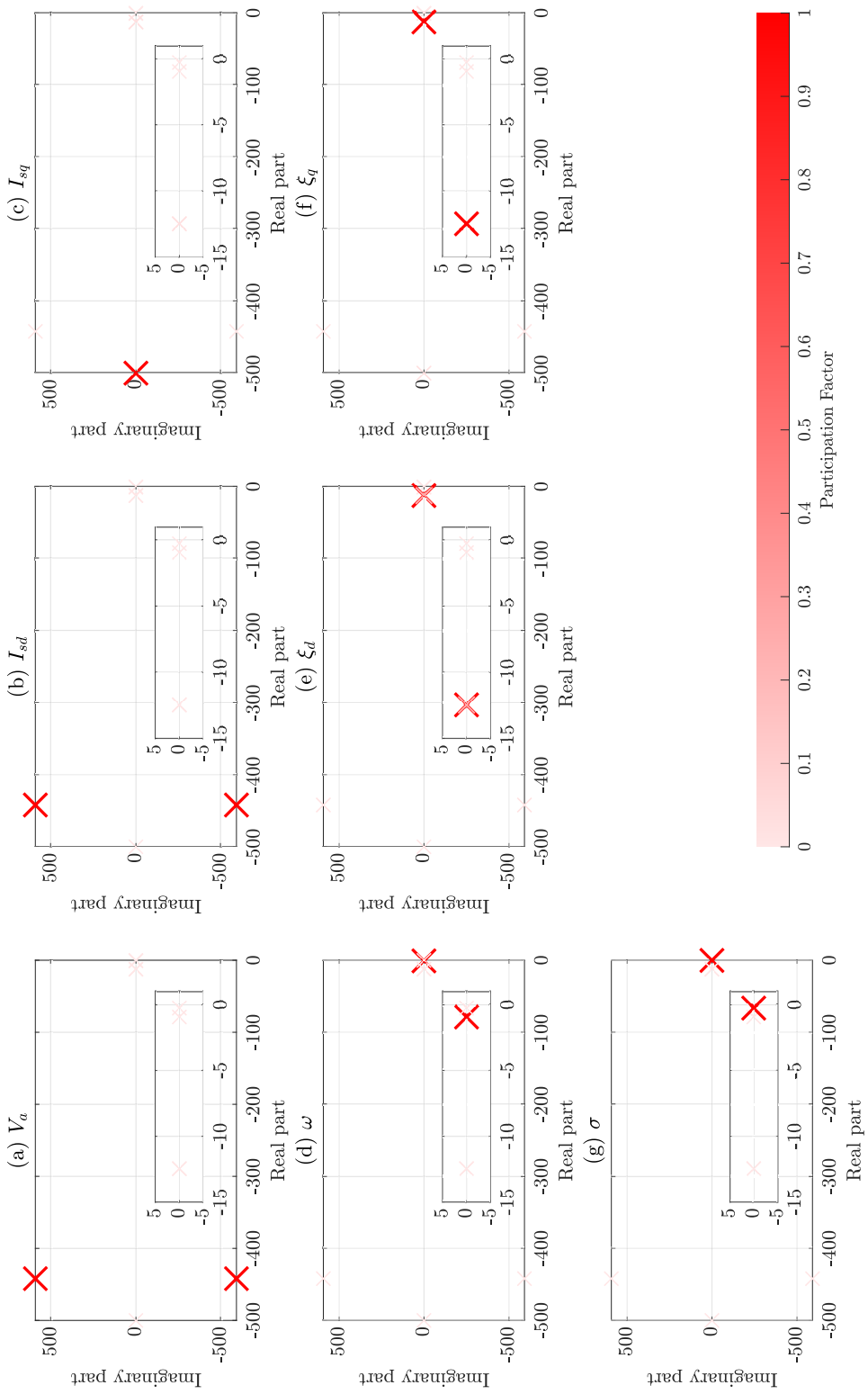

Figure 4.1: Eigenvalues of the averaged high-order model's Jacobian matrix, with each eigenvalue color coded according to the participation factor of: (a) Va, (b) I_{sd}, (c) I_{sq}, (d) ω, (e) ξ_d, (f) ξ_q, and (g) σ.

Table 4.1: Model Parameters

Symbol	**Value**	**Unit**
k	4	N/A
L	0.73E-3	H
R	9.1E-3	Ω
C	10E-3	F
E_0	1.24	kV
f_0	20	Hz
V_{dc}	7.8	kV
$k_{\mathrm{p}i}$	0.975	Ω
$k_{\mathrm{i}i}$	1.15	F^{-1}
$k_{\mathrm{p}p}$	-0.365	V
$k_{\mathrm{i}p}$	-4.55	1/Vs
S	10	MW
J	28.7E6	kgm^2
p	240	N/A
ρ	1.15	m/s
A	6724π	m^2
R_{blade}	82	m

Table 4.2: Initial Conditions

Symbol	**Value**	**Unit**
V_a	2479.28	kV
I_{sd}	1460.21	A
I_{sq}	0	A
ω	114.60	rad/s
ξ_d	4	A s
ξ_q	2.92	A s
σ	9.73E6	W s
ν	11	m/s

accuracy. Results for I_{sq} and ξ_q are not displayed because their values are approximately zero regardless of input.

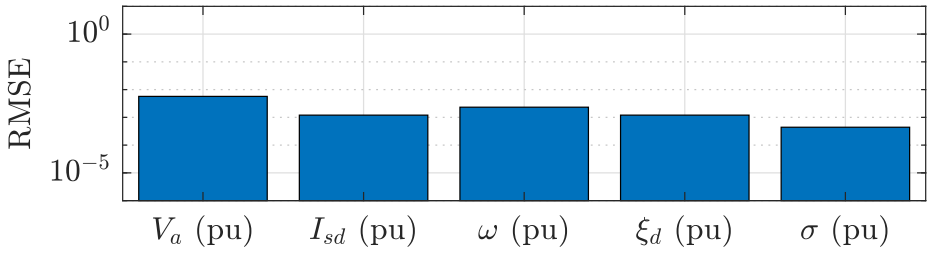

Figure 4.2: RMSE of the reduced-order model relative to the averaged high-order model.

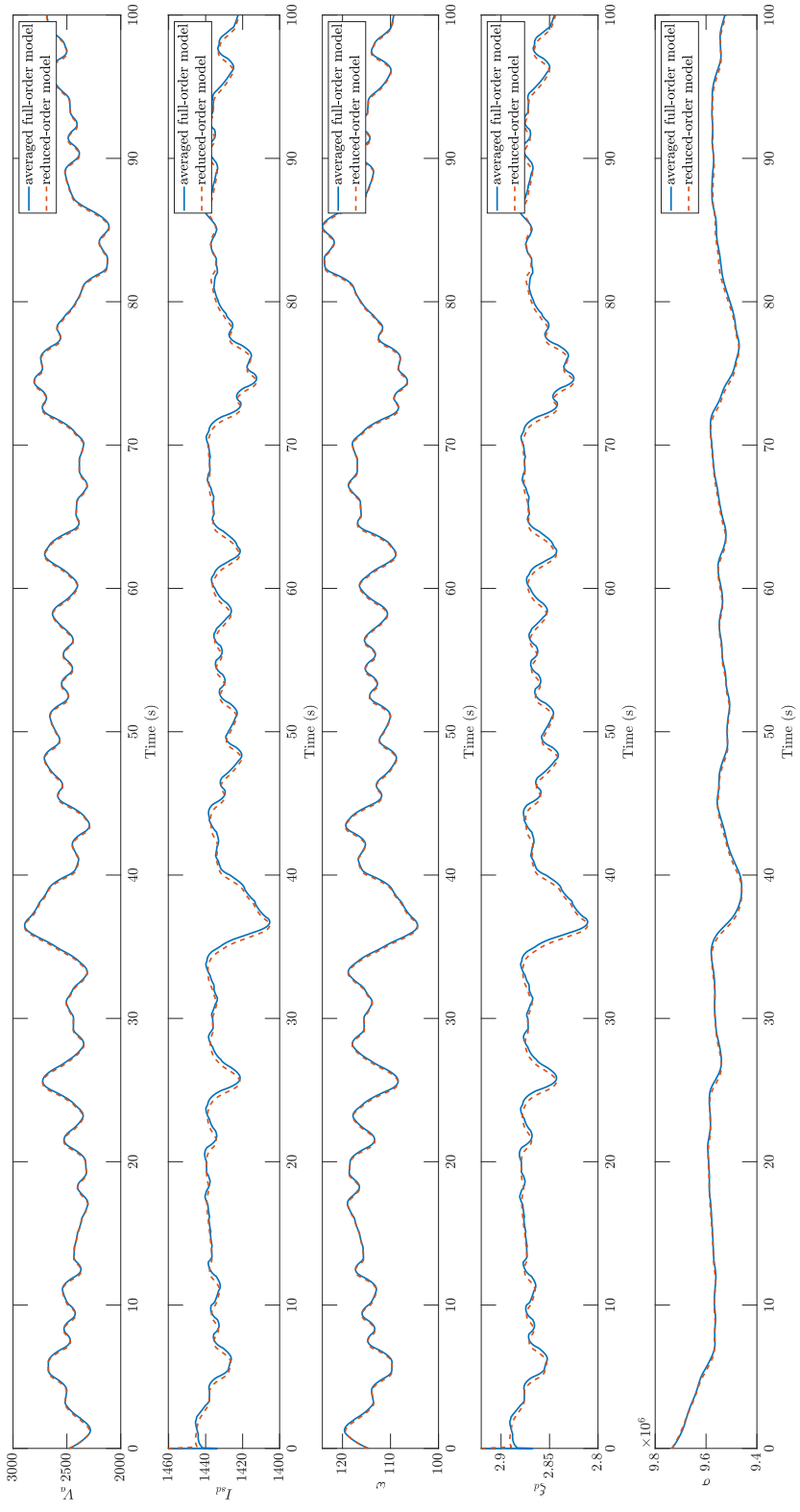

Figure 4.3: State variables value comparison of averaged high-order and reduced-order model.

CHAPTER 5

EXPECTED POWER OUTPUT

Power generated from off-shore wind turbines can be anticipated by knowing the expected wind statistic of the location of the turbine. This knowledge ensures that wind turbines are not placed in sub-optimal locations where their capabilities are not fully realized. It also allows for proper planning of power allocation for residential and industrial customers. The expected power output of this wind turbine over the next 30 years is calculated using an approximation of a possible off-shore wind profile and power output of the turbine in its different available states.

5.1 Wind Profile

For all wind turbines, the wind profile of the region where they are located is needed to predict how much wind the turbine will experience and in turn, how much power it will generate in its lifetime. The Weibull distribution, a two-parameter function, is often a good approximation for the wind speed distribution and can provide data points for various wind energy calculations [38]. The probability density function of a Weibull random variable, x, is [39]:

$$pdf(x) = \frac{h}{a}\left(\frac{x}{a}\right)^{h-1} e^{-(x/a)^k}, \tag{5.1}$$

where $h > 0$ is the shape parameter and $a > 0$ is the scale parameter. The wind speeds used for the simulation were generated using the MATLAB function, *wblrnd(.)*, that generated an array of 500 random numbers from a Weibull distribution with $a = 10.13$, and $h = 2.1$. These parameters were chosen because these parameters represent an average wind speed of around 9 m/s in most off-shore regions around the world close to shorelines and are

taken from [40]. A histogram of the random numbers generated can be seen in Fig. 5.1.

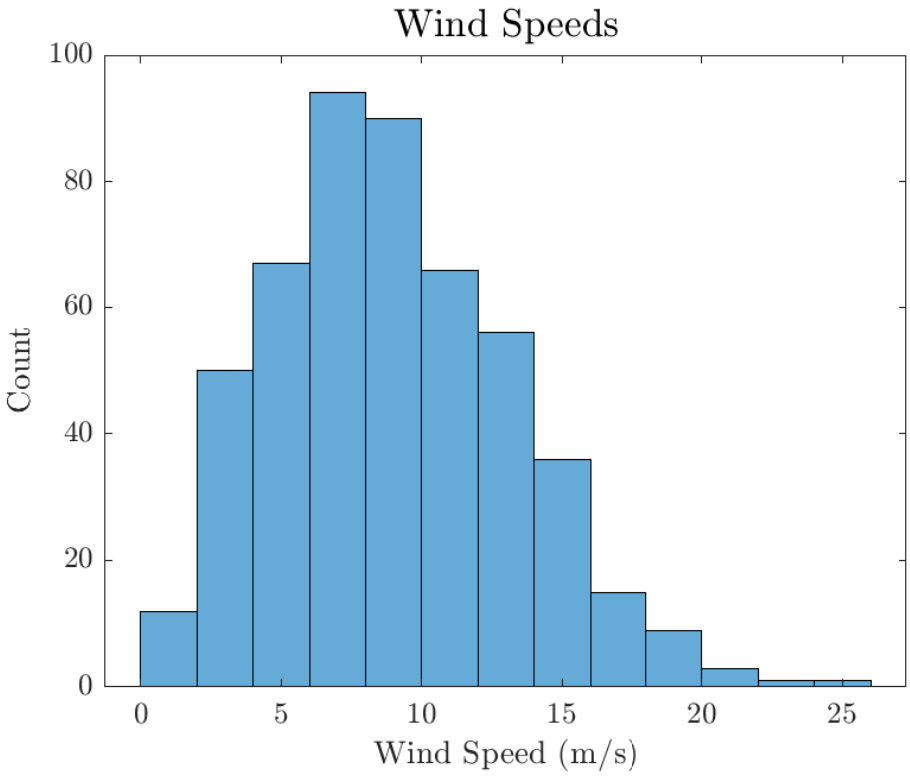

Figure 5.1: Weibull distribution of wind speeds used for power output calculation.

5.2 Power Output

To determine the expected output of power by the 10 MW integrated generator-rectifier off-shore wind turbine over a 30 year period, its power output for every available state must be determined. The reduced order models from section 4.2 were fed with a number of normally distributed wind speeds, with varianc, 0.1, and mean, the values from the Weibull distribution in section 5.1. Each wind speed was tested with seed 1 to 20, and sample time 0.1, for 100 seconds using MATLAB Simulink, resulting in 10,000 unique realizations of wind speeds the wind turbine could experience. The power output from the reduced-order model for all these realizations is then averaged. This process is done for the four major sets of available states the integrated-generator

rectifier system can be in:

- k = 1: one active rectifier available and three passive rectifiers unavailable.
- k = 2: one active rectifier available, one passive rectifier available, and two passive rectifiers unavailable.
- k = 3: one active rectifier available, two passive rectifiers available, and one passive rectifier unavailable.
- k = 4: one active rectifier available and three passive rectifiers available.

The results of this averaging can be seen in Fig. 5.2. The probabilities of these major sets, using repair strategy 2 from section 3.2.3, are presented in Table 5.1. As seen from the table and figure, we can expect an average output of about 5 MW of power over 30 years from this off-shore wind turbine design.

Table 5.1: Probabilities of Available States

No. of functioning rectifiers	Probability States	Value
k = 1	π_{10}, π_{11}, π_{12}	0.0000
k = 2	π_7, π_8, π_9	0.0000
k = 3	π_4, π_5, π_6	0.0000
k = 4	π_1, π_2, π_3	0.9998

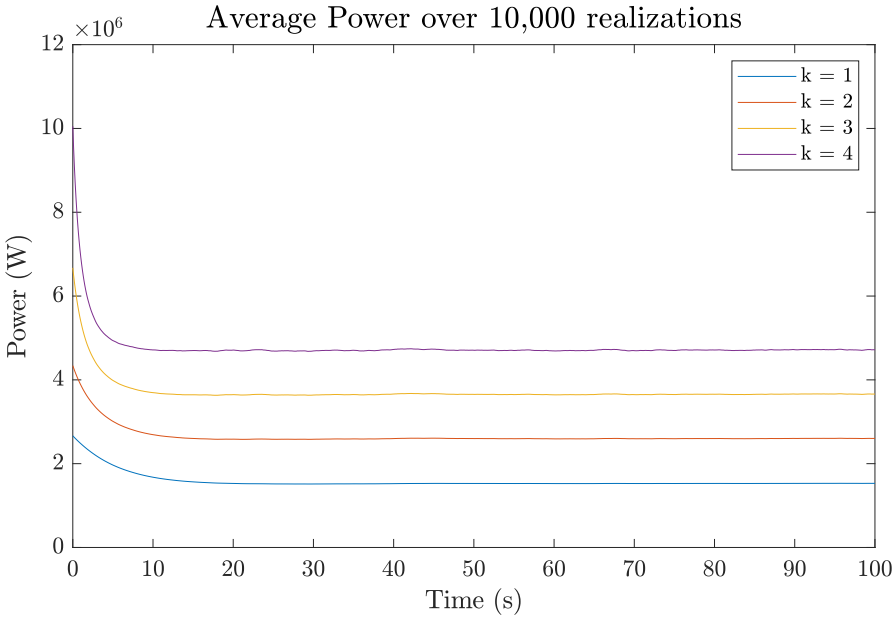

Figure 5.2: Expected power output of the integrated generator-rectifier systems with various configurations of failed passive rectifiers.

CHAPTER 6

CONCLUDING REMARKS

In this thesis, an integrated generator-rectifier system for off-shore wind-energy conversion systems is introduced. This system is outfitted with various power converter architectures. A baseline architecture is introduced, as well as two proposed architectures, both of which contain passive rectifiers, and one of which contains an additional bypass mechanism to isolate failed passive rectifiers. Each architecture also contains an active rectifier and auxiliary systems. The differences in architecture affect its fault tolerance which in turn affects all the reliability metrics.

Markov reliability models of these architectures are presented. A reduction in component failure rates for Architectures 2 and 3 is observed because of the difference in operating voltage of their active rectifiers compared to that of Architecture 1. The models are used to calculate the converter and system-level failure rates for each converter architecture. The results show that Architectures 2 and 3 perform at least an order of magnitude better than Architecture 1. Architecture 3 performs even better than Architecture 2 because the bypass mechanism ensures that Architecture 3 remains operational after failures in any passive rectifier. The failure rates of the active and passive switches are determined to have the biggest effect on the system-level failure rate of all the architectures. Architecture 3 also shows a significant reduction in failure rate for the scaled component failure rates compared to Architectures 1 and 2.

Markov availability models with differing repair strategies for each architecture are created. Availability of the architectures is calculated using the Chapman-Kolmogorov equation, and Architecture 3 is shown to have the highest availability. Another point of note is that the most aggressive repair strategy for Architecture 1 still results in a lower availability than the most conservative repair strategy for Architecture 2. Sensitivity analysis is performed on the component failure and repair rates, and similar to the Markov

reliability models, the failure and repair rates associated with the active and passive switches have the biggest effect on the availability of the system. Architecture 3 is shown to perform better than its counterparts, even after scaling of component failure and repair rates.

An averaged high-order dynamical model of the integrated generator-rectifier system is presented. Equations for the passive and active rectifiers, control architecture, and mechanical parts of the system were used to create a state space model. Via singular perturbation analysis, this seventh-order model was reduced to a second-order model with multiple algebraic equations. This reduced-order model is compared to the averaged high-order model, having much shorter simulation time while maintaining a high level of accuracy.

The reduced-order model is simulated and used to determine the expected power output of the off-shore wind turbine based on a wind profile determined by a Weibull distribution. Power output is calculated for the cases of 1, 2, 3, and 4 functioning rectifiers. An average output of about 5 MW of power over 30 years is expected.

The novel integrated generator-rectifier system with bypass mechanism is shown to have the highest performances in reliability and availability metrics. It also ensures power production during passive rectifier failure, which is of high importance for off-shore wind turbines. This novel approach presents a new option for high power off-shore wind turbines. This kind of technology ensures that the push for worldwide electrification and reduction of CO_2 emissions with increased renewable energy generation is feasible.

REFERENCES

[1] United Nations, "Sustainable development goals knowledge platform," *Transforming our World: The 2030 Agenda for Sustainable Development*, 2015.

[2] "Global energy review 2020." 2020, IEA, Paris. [Online]. Available: https://www.iea.org/reports/global-energy-review-2020

[3] R. Thresher, M. Robinson, and P. Veers, "To capture the wind," *IEEE Power and Energy Magazine*, vol. 5, no. 6, pp. 34–46, 2007. [Online]. Available: www.scopus.com

[4] U.S. Dept. of Energy, Office of Energy Efficiency and Renewable Energy, "20% Wind Energy by 2030: Increasing Wind Energy's Contribution to U.S. Electricity Supply," 2008.

[5] C. W. Zheng, C. Y. Li, J. Pan, M. Y. Liu, and L. L. Xia, "An overview of global ocean wind energy resource evaluations," *Renewable and Sustainable Energy Reviews*, vol. 53, pp. 1240–1251, 2016. [Online]. Available: https://www.sciencedirect.com/science/article/pii/S1364032115010333

[6] J. Kaldellis and M. Kapsali, "Shifting towards offshore wind energy—recent activity and future development," *Energy Policy*, vol. 53, pp. 136–148, 2013. [Online]. Available: https://www.sciencedirect.com/science/article/pii/S0301421512008907

[7] Siemens Gamesa, "SG 10.0-193dd offshore wind turbine," 2019. [Online]. Available: https://www.siemensgamesa.com/-/media/siemensgamesa/downloads/en/products-and-services/offshore/brochures/siemens-gamesa-offshore-wind-turbine-sg-10-0-193-dd-en-double.pdf

[8] GE Renewable Energy, "Haliade-X 12 MW Offshore Wind Turbine Platform." [Online]. Available: https://www.ge.com/renewableenergy/wind-energy/offshore-wind/haliade-x-offshore-turbine

[9] Vestas American Wind Technology, "Vestas V164-10.0 MW." [Online]. Available: https://us.vestas.com/en-us/products/offshore/V164-10-0-MW

[10] A. Yazdani and R. Iravani, "A neutral-point clamped converter system for direct-drive variable-speed wind power unit," *IEEE Trans. Energy Convers.*, vol. 21, no. 2, p. 596–607, June 2006.

[11] M. L. F. Blaabjerg and K. Ma, "Power electronics converters for wind turbine systems," *IEEE Trans. Ind. Appl.*, vol. 48, no. 2, p. 708–719, Mar./Apr. 2012.

[12] S. Li, T. A. Haskew, R. P. Swatloski, and W. Gathing, "Optimal and direct-current vector control of direct-driven pmsg wind turbines," *IEEE Trans. Power Electron.*, vol. 27, no. 5, p. 2325–23379, May 2012.

[13] M. Chinchilla, S. Arnaltes, and J. C. Burgos, "Control of permanent-magnet generators applied to variable-speed wind-energy systems connected to the grid," *IEEE Trans. Energy Convers.*, vol. 21, no. 1, p. 130–135, Mar. 2006.

[14] F. Rong, G. Wu, X. Li, S. Huang, and B. Zhou, "ALL-DC offshore wind farm with series-connected wind turbines to overcome unequal wind speeds," *IEEE Trans. Power Electron.*, vol. 34, no. 2, p. 1370–1381, Feb. 2019.

[15] S. Ye, D. Zhou, X. Yao, and F. Blaabjerg, "Component-level reliability assessment of a direct-drive pmsg wind power converter considering two terms of thermal cycles and the parameter sensitivity analysis," *IEEE Trans. Power Electron.*, vol. 36, no. 9, p. 10037–10050, Sep. 2021.

[16] P. T. Huynh, P. J. Wang, and A. Banerjee, "An integrated permanent magnet-synchronous generator-rectifier architecture for limited-speed range applications," *IEEE Trans. Power Electron.*, vol. 35, no. 5, p. 4767–4779, May 2020.

[17] P. Huynh and A. Banerjee, "Active voltage-ripple compensation in an integrated generator-rectifier system," *IEEE Trans. Power Electron.*, vol. 36, no. 2, p. 2270–2282, Feb. 2021.

[18] P. T. Huynh, S. Tungare, and A. Banerjee, "Maximum power point tracking for wind turbine using integrated generator-rectifier systems," *IEEE Transactions on Power Electronics*, pp. 1–1, 2020.

[19] C. A. Walford, "Wind turbine reliability: Understanding and minimizing wind turbine operation and maintenance costs," Sandia National Laboratories (SNL), Albuquerque, NM, Tech. Rep. SAND2006-1100, 2006.

[20] J. Carroll, A. McDonald, and D. McMillan, "Reliability comparison of wind turbines with DFIG and PMG drive trains," *IEEE Transactions on Energy Conversion*, vol. 30, no. 2, pp. 663–670, June 2015.

[21] P. Huynh, S. Sirimanna, J. Mok, D. Lee, O. Ajala, S. Linares, D. Mulas, K. Haran, A. Dominguez-Garcia, G. Gross, and A. Banerjee, "Integrated generator-rectifier co-design for offshore wind turbines," in *Proc. of the IEEE Energy Convers. Congr. Expo. (ECCE)*, 2020, pp. 4194–4201.

[22] N. Celanovic and D. Boroyevich, "A comprehensive study of neutral-point voltage balancing problem in three-level neutral-point-clamped voltage source PWM inverters," *IEEE Trans. Power Electron.*, vol. 15, no. 2, pp. 242–249, 2000.

[23] J. Norris, *Markov Chains*, ser. Cambridge Series in Statistical and Probabilistic Mathematics. Cambridge: Cambridge University Press, 1997.

[24] G. Grimmett and D. Stirzaker, *Probability and Random Processes*. Oxford and New York: Oxford University Press, 2001. [Online]. Available: http://www.worldcat.org/search?qt=worldcat_org_all&q=9780198572220

[25] A. D. Domínguez-García, *Large-Scale System Analysis Under Uncertainty: With Electric Power Applications*. Cambridge University Press, 2022.

[26] H. Wang, D. A. Nielsen, and F. Blaabjerg, "Degradation testing and failure analysis of dc film capacitors under high humidity conditions," *Microelectronics Reliability*, vol. 55, no. 9, pp. 2007 – 2011, 2015.

[27] "DC Link Film Capacitors Datasheets," Mouser Electronics. [Online]. Available: https://www.mouser.com/Passive-Components/Capacitors/Film-Capacitors/Datasheets/_/N-9x371?P=1yzvdnf

[28] J. Angus and A. Ward, *Electronic Product Design*, ser. Tutorial Guides in Electronic Engineering. Taylor & Francis, 1996.

[29] I. Bazovsky, *Reliability Theory and Practice*, ser. Dover Civil and Mechanical Engineering Series. Dover Publications, 2004.

[30] "Vishay Semiconductors," Vishay. [Online]. Available: https://www.vishay.com/

[31] J. Carroll, A. McDonald, and D. McMillan, "Failure rate, repair time and unscheduled O & M cost analysis of offshore wind turbines," *Wind Energy*, vol. 19, no. 6, pp. 1107–1119, August 2015.

[32] U. Häger, C. Rehtanz, and N. Voropai, *Monitoring, Control and Protection of Interconnected Power Systems*. Springer, 2014.

[33] J. G. Kassakian, M. F. Schlecht, and G. C. Verghese, *Principles of Power Electronics*. Addison-Wesley Publishing Company, 1991.

[34] S. M. R. Kazmi, H. Goto, H. Guo, and O. Ichinokura, "A novel algorithm for fast and efficient speed-sensorless maximum power point tracking in wind energy conversion systems," *IEEE Trans. Ind. Electron.*, vol. 58, no. 1, pp. 29–36, Jan 2011.

[35] C. H. Houpis and M. Garcia-Sanz, *Wind Energy Systems: Control Engineering Design*. CRC Press, 2012.

[36] P. V. Kokotovic, J. O'Reilly, and H. K. Khalil, *Singular Perturbation Methods in Control: Analysis and Design*. USA: Academic Press, Inc., 1986.

[37] I. J. Perez-Arriaga, G. C. Verghese, and F. C. Schweppe, "Selective modal analysis with applications to electric power systems, Part I: Heuristic introduction," *IEEE Transactions on Power Apparatus and Systems*, vol. PAS-101, no. 9, pp. 3117–3125, 1982.

[38] J. Seguro and T. Lambert, "Modern estimation of the parameters of the Weibull wind speed distribution for wind energy analysis," *Journal of Wind Engineering and Industrial Aerodynamics*, vol. 85, no. 1, pp. 75–84, 2000. [Online]. Available: https://www.sciencedirect.com/science/article/pii/S0167610599001221

[39] A. Papoulis and S. U. Pillai, *Probability, Random Variables, and Stochastic Processes*, 4th ed. Boston: McGraw Hill, 2002. [Online]. Available: http://www.worldcat.org/search?qt=worldcat_org_all&q=0071226613

[40] M. Garcia-Sanz, "A metric space with lcoe isolines for research guidance in wind and hydrokinetic energy systems," *Wind Energy*, vol. 23, no. 2, Feb 2020.